PLoS COMPUTATIONAL BIOLOGY

Simulation of the Undiseased Human Cardiac Ventricular Action Potential: Model Formulation and Experimental Validation

Thomas O'Hara[1], **László Virág**[2], **András Varró**[2,3], **Yoram Rudy**[1]*

1 Cardiac Bioelectricity and Arrhythmia Center, Department of Biomedical Engineering, Washington University in St. Louis, St. Louis, Missouri, United States of America, **2** Department of Pharmacology and Pharmacotherapy, University of Szeged, Szeged, Hungary, **3** Division of Cardiovascular Pharmacology, Hungarian Academy of Sciences, Szeged, Hungary

Abstract

Cellular electrophysiology experiments, important for understanding cardiac arrhythmia mechanisms, are usually performed with channels expressed in non myocytes, or with non-human myocytes. Differences between cell types and species affect results. Thus, an accurate model for the undiseased human ventricular action potential (AP) which reproduces a broad range of physiological behaviors is needed. Such a model requires extensive experimental data, but essential elements have been unavailable. Here, we develop a human ventricular AP model using new undiseased human ventricular data: Ca^{2+} versus voltage dependent inactivation of L-type Ca^{2+} current (I_{CaL}); kinetics for the transient outward, rapid delayed rectifier (I_{Kr}), Na^+/Ca^{2+} exchange (I_{NaCa}), and inward rectifier currents; AP recordings at all physiological cycle lengths; and rate dependence and restitution of AP duration (APD) with and without a variety of specific channel blockers. Simulated APs reproduced the experimental AP morphology, APD rate dependence, and restitution. Using undiseased human mRNA and protein data, models for different transmural cell types were developed. Experiments for rate dependence of Ca^{2+} (including peak and decay) and intracellular sodium ($[Na^+]_i$) in undiseased human myocytes were quantitatively reproduced by the model. Early afterdepolarizations were induced by I_{Kr} block during slow pacing, and AP and Ca^{2+} alternans appeared at rates $>$200 bpm, as observed in the nonfailing human ventricle. Ca^{2+}/calmodulin-dependent protein kinase II (CaMK) modulated rate dependence of Ca^{2+} cycling. I_{NaCa} linked Ca^{2+} alternation to AP alternans. CaMK suppression or SERCA upregulation eliminated alternans. Steady state APD rate dependence was caused primarily by changes in $[Na^+]_i$, via its modulation of the electrogenic Na^+/K^+ ATPase current. At fast pacing rates, late Na^+ current and I_{CaL} were also contributors. APD shortening during restitution was primarily dependent on reduced late Na^+ and I_{CaL} currents due to inactivation at short diastolic intervals, with additional contribution from elevated I_{Kr} due to incomplete deactivation.

Citation: O'Hara T, Virág L, Varró A, Rudy Y (2011) Simulation of the Undiseased Human Cardiac Ventricular Action Potential: Model Formulation and Experimental Validation. PLoS Comput Biol 7(5): e1002061. doi:10.1371/journal.pcbi.1002061

Editor: Andrew D. McCulloch, University of California San Diego, United States of America

Received December 20, 2010; **Accepted** April 5, 2011; **Published** May 26, 2011

Copyright: © 2011 O'Hara et al. This is an open-access article distributed under the terms of the Creative Commons Attribution License, which permits unrestricted use, distribution, and reproduction in any medium, provided the original author and source are credited.

Funding: This work was supported by NIH/National Heart, Lung, and Blood Institute grants R01-HL049054-18 and R01-HLR01033343-26, Fondation Leducq Award to the Alliance for CaMK Signaling in Heart Disease, and National Science Foundation grant CBET-0929633 (to YR); Hungarian Scientific Research Fund grant OTKA CNK-77855, National Office for Research and Technology grant - National Technology Programme (TECH_08_A1_CARDIO08), and National Development Agency grant TÁMOP-4.2.2-08/1-2008-0013 (to AV); Hungarian Ministry of Health grant ETT 302-03/2009 (to LV); American Heart Association Predoctoral Fellowship 0815539G (to TO). Y. Rudy is the Fred Saigh Distinguished Professor at Washington University. The funders had no role in study design, data collection and analysis, decision to publish, or preparation of the manuscript.

Competing Interests: The authors have declared that no competing interests exist.

* E-mail: rudy@wustl.edu

Introduction

The first step toward preventing sudden cardiac death is understanding the basic mechanisms of ventricular arrhythmias at the level of ion channel currents and the single myocyte action potential (AP), using both experiments[1] and theoretical models[2]. Obtaining ventricular myocytes from human hearts for the study of arrhythmia mechanisms is both rare and technically challenging. Consequently, these mechanisms are usually studied with human channels expressed in non myocytes, or with non human (rodent or other mammalian) myocytes. However, these approaches have limitations, because functionally important accessory subunits and anchoring proteins native to ventricular myocytes[3] are absent in expression systems, and even among mammalian ventricular myocytes, ion channel kinetics[4,5,6] and consequently arrhythmia mechanisms are strongly species dependent.

These issues limit the applicability of results from animal studies to human cardiac electrophysiology and clinical arrhythmia[7]. Measurements from undiseased human ventricular myocytes are a requisite for understanding human cell electrophysiology. Here, we present data from over 100 undiseased human hearts for steady state rate dependence, and restitution of the ventricular AP. Importantly, we also obtained essential new measurements for the L-type Ca^{2+} current, K^+ currents, and Na^+/Ca^{2+} exchange current from undiseased human ventricle. These previously unavailable data are critically important for correct formulation of mathematical models for simulation of electrophysiology and cellular arrhythmia mechanisms[8]. Using the new data together with previously published experiments, a detailed mathematical model of undiseased human ventricular myocyte electrophysiology and Ca^{2+} cycling was developed and thoroughly validated over the entire range of physiological frequencies. This model is referred to

Author Summary

Understanding and preventing irregular heart rhythms that can lead to sudden death begins with basic research regarding single cell electrical behavior. Most of these studies are performed using non-human cells. However, differences between human and non-human cell properties affect experimental results and invoke different mechanisms of responses to heart rate changes and to drugs. Using essential and previously unavailable experimental data from human hearts, we developed and validated an accurate mathematical model of the human cardiac cell. We compared cellular behaviors and mechanisms to an extensive dataset including measurements from more than 100 undiseased human hearts. The model responds to pacing rate and premature beats as in experiments. At very fast pacing rates, beat to beat alternations in intracellular calcium concentration and electrophysiological behavior were observed as in human heart experiments. In presence of drug block, arrhythmic behavior was observed. The basis for these and other important rhythmic and irregular rhythm behaviors was investigated using the model.

as the ORd (O'Hara-Rudy dynamic) model throughout the text. Model comparisons are conducted with the ten Tusscher-Panfilov (TP) model[9], and the Grandi-Bers (GB) model[10].

The ORd model was used to describe cellular electrophysiology mechanisms specific to human ventricular myocytes. Underlying mechanisms of AP duration (APD) rate dependence and APD restitution were investigated. The effects of Ca^{2+}/calmodulin-dependent protein kinase II (CaMK) on known ionic current and Ca^{2+} cycling targets were incorporated and studied. Early afterdepolarizations (EADs) and alternans were reproduced by the model. These are important arrhythmogenic phenomena that must be reproduced in order to study the mechanisms of cardiac arrhythmias in human and simulate clinical interventions such as drugs.

Results

Throughout, new undiseased human ventricle experimental data are represented by white circles or white squares for isolated myocyte or small tissue preparation measurements, respectively. Previously published nonfailing human ventricle experimental data are shown with black symbols. Other data classification schemes are provided case by case in figure legends.

Formulation, Validation and Properties of Simulated Currents: L-type Ca^{2+} Current (I_{CaL})

Data for I_{CaL} in the undiseased human ventricle are from Magyar et al.[11] and Fulop et al.[12] (both at 37°C, model validation in Figure 1C). Magyar et al. measured steady state activation, steady state inactivation, and the current voltage (I–V) curve. Fulop et al. measured recovery from inactivation. However, neither study separated Ca^{2+} dependent inactivation (CDI) from voltage dependent inactivation (VDI). In fact, no published data are available which separate CDI and VDI in the undiseased or nonfailing human ventricle. For this measurement, we made new recordings in undiseased human ventricular myocytes at 37°C (Figure 1, current traces and white circles).

Measurements were carried out with Ca^{2+} as charge carrier, allowing both CDI and VDI, or with Ba^{2+} as charge carrier, allowing only VDI. Results for Sr^{2+} were similar to those for Ba^{2+}. From holding potential of −60 mV, 75 ms steps were to potentials ranging from −40 to +50 mV (10 mV increments, 3 second interpulse interval, Figure 1A). 75 ms was sufficient for comparison of CDI and VDI, since it is in the early phase of decay in which CDI effects are most prominent[13]. Simulated current traces for CDI+VDI and for VDI–alone were similar to the experiments.

Fractional remaining current (FRC, at time t and voltage V_m, $FRC(t,V_m) = I(t,V_m)/I_{peak}(V_m)$) quantified the voltage and time dependence of inactivation for comparison between charge carriers. Figure 1B compares FRC for Ba^{2+} (experiments top left, simulations right), and Ca^{2+} (experiments bottom left, simulations right). With Ba^{2+} as the charge carrier, FRC monotonically decreased with increasing voltage at all times after peak current. This finding is consistent with dependence of inactivation on voltage alone. In contrast, for Ca^{2+} currents, FRC did not decrease monotonically with increasing voltage. Rather, Ca^{2+} current FRC curves appear to be effectively voltage independent. FRC for CDI+VDI was statistically different from FRC for VDI-alone at the more hyperpolarized potentials (−20 to 0 mV, unpaired two-tailed t-test, $p < 0.01$). Ca^{2+} ions caused additional inactivation at these voltages, where VDI-alone was relatively weak. Since the only difference between Ca^{2+} and Ba^{2+} cases was the charge carrier, it follows that Ca^{2+} ions themselves were the source of the additional inactivation. This is evidence that currents carried by Ba^{2+} inactivate due to VDI only, while Ca^{2+} currents inactivate due to both VDI and CDI[14]. There is evidence that Ba^{2+} can cause ion dependent inactivation[15]. However, Ba^{2+}-dependent inactivation was estimated to be 100-fold weaker than CDI[16], and its effects were not appreciable in FRC experiments.

To modulate VDI versus CDI in the model, the n gate was introduced, the value of which represents the fraction of channels operating in CDI mode. Under physiological conditions, I_{CaL} inactivation is caused by a combination of both CDI and VDI. That is, n is between 0 (all VDI) and 1 (all CDI). This model was based on experiments by Kim et al.[17], where CDI was observed to function as a faster VDI, activated by elevated Ca^{2+}. Thus, both CDI and VDI are voltage dependent. The rate of decay in CDI mode is faster than that in VDI mode. The Mahajan et al.[18] and Decker et al.[19] I_{CaL} models work similarly.

The n gate is diagrammed in Figure 1E. Rates k_1 and k_{-1} represent binding/unbinding of Ca^{2+} to channel bound calmodulin (CaM)[20]. There are four identical binding sites. Rates k_2 and k_{-2} represent activation/deactivation of CDI mode (black circle, asterisk), which occurs when all Ca^{2+} binding sites are occupied. We considered that the four Ca^{2+} binding transitions are in rapid equilibrium and solved the reversible two state reaction of Ca^{2+}/CaM binding and CDI mode activation to obtain the differential equation describing the n gate (Supplement Text S1, page 10).

In both CDI and VDI modes, there are two weighted time constants for inactivation (time constant weighting described in Methods). We determined time constants for CDI and n gate kinetics in an attempt to represent the shape and magnitude of the FRC measurements (i.e. CDI reduced FRC, particularly at negative potentials). Time constants for VDI gates were determined by inactivation of Ba^{2+} currents (Figure 1C). AP clamp simulations using the formulated I_{CaL} model were similar to AP clamp experiments, where I_{CaL} was defined as the 1 μM nisoldipine sensitive current (Figure 1D). Specifically, currents showed spike and dome morphology. In experiments, peak current was −3.0 μA/μF. It was −2.7 μA/μF in simulations. Fast inactivation was 2.5 fold faster when phosphorylated by CaMK, similar to the Decker et al. dog I_{CaL} model[19] and as measured experimentally[21].

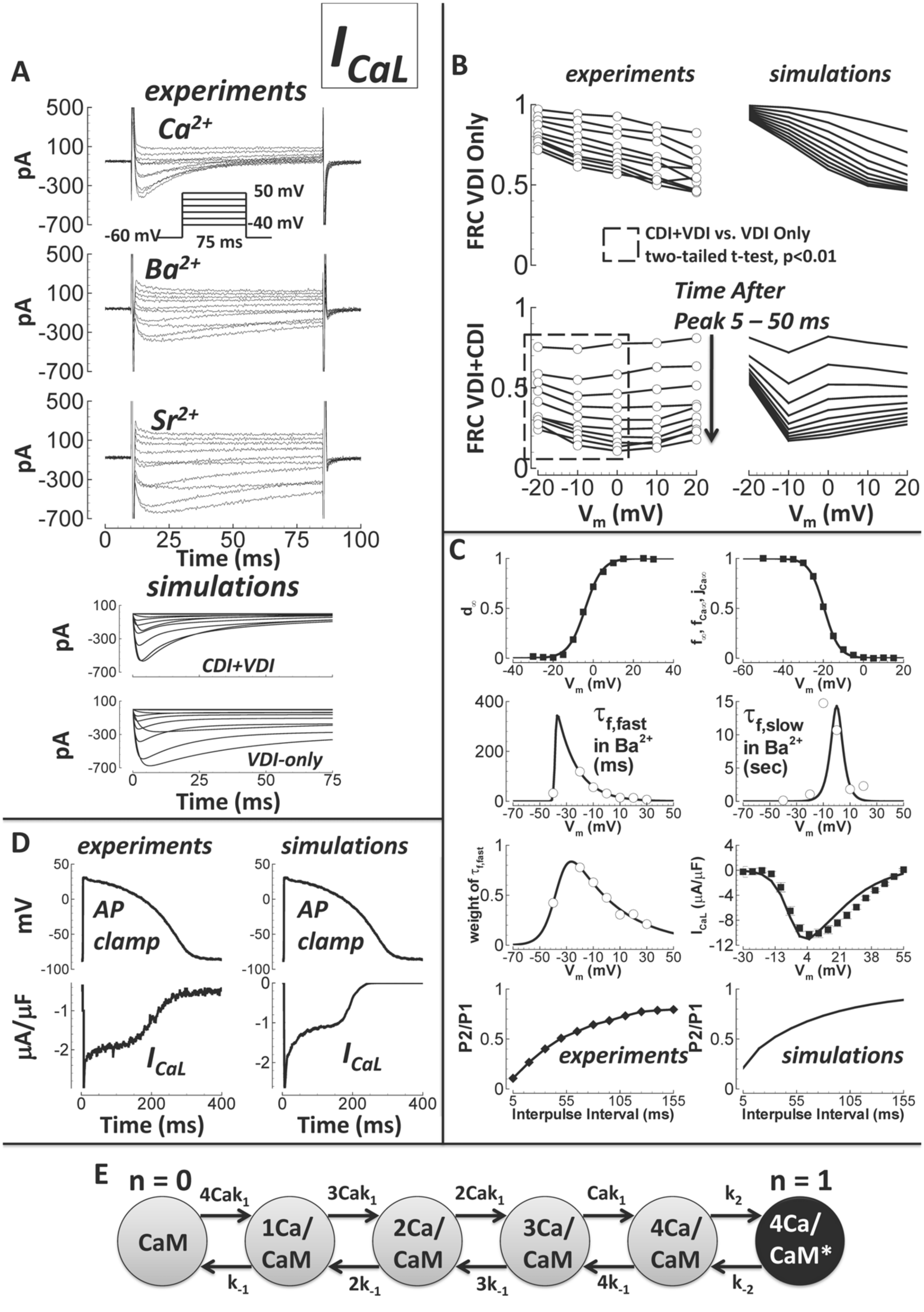
I_{CaL}
A
experiments
Ca²⁺
Ba²⁺
Sr²⁺
500
100
-300
-700
pA
50 mV
-40 mV
-60 mV
75 ms
0
25
50
75
100
Time (ms)
simulations
CDI+VDI
VDI-only
B
experiments
simulations
FRC VDI Only
FRC VDI+CDI
CDI+VDI vs. VDI Only
two-tailed t-test, p<0.01
Time After
Peak 5 – 50 ms
-20
-10
0
10
20
Vm (mV)
C
d∞
f∞, fCa∞, jCa∞
τf,fast in Ba²⁺ (ms)
τf,slow in Ba²⁺ (sec)
weight of τf,fast
ICaL (μA/μF)
P2/P1
experiments
simulations
Interpulse Interval (ms)
D
experiments
simulations
AP clamp
mV
μA/μF
ICaL
Time (ms)
E
n = 0
n = 1
4Cak1
3Cak1
2Cak1
Cak1
k2
CaM
1Ca/CaM
2Ca/CaM
3Ca/CaM
4Ca/CaM
4Ca/CaM*
k-1
2k-1
3k-1
4k-1
k-2

Figure 1. Undiseased human I_{CaL} experiments and model validation. A) Experiments: I_{CaL} traces for currents carried by Ca^{2+} (top), Ba^{2+} (middle), and Sr^{2+} (bottom). The voltage protocol is below the Ca^{2+} traces. Ca^{2+} current decay was visibly more rapid than decay for Ba^{2+} or Sr^{2+} currents. Simulations: I_{CaL} in response to the same voltage protocol with CDI (CDI+VDI, top), and without CDI (VDI-only, bottom). B) Experimental data are on the left (white circles, N = 5, from 3 hearts). Simulation results are on the right (solid lines). FRC is fractional remaining current. Times after peak current shown are from 5 to 55 ms, in 5 ms steps (indicated by arrow). Top left) Experiments showing the voltage and time dependence of FRC with Ba^{2+} as charge carrier (VDI only). Top right) Simulations of FRC, with n−gate = 0 (representing VDI only; see text and panel E). Bottom left) Experiments showing FRC with Ca^{2+} as charge carrier (CDI and VDI are concurrent). FRC for CDI+VDI was significantly smaller at more hyperpolarized potentials ($V_m = -20$ to 0 mV, dashed box) than FRC for VDI-alone. Bottom right) Simulations of FRC with free running n gate, allowing both CDI and VDI to occur. C) Data are from Magyar et al.[11] (black squares), Fulop et al.[12] (black diamonds), and previously unpublished (white circles, N = 5, from 3 hearts). Simulation results are solid lines. From left to right, top to bottom: steady state activation, steady state inactivation, fast time constant for VDI, slow time constant for VDI, relative weight of the fast component for VDI, I–V curve, experiments showing recovery from inactivation, and corresponding simulations. D) Human AP clamp waveform, used to elicit 1 μM nisoldipine sensitive current (I_{CaL}, experiments, left) and comparison to simulations using the same AP clamp (right). E) Schematic diagram for the n gate, representing the fraction of L-type channels undergoing CDI. Calmodulin (CaM) is constitutively attached to the L-type channel. Ca^{2+} ions bind to CaM (on-rate k_1 and off-rate k_{-1}). With Ca^{2+} ions bound, the Ca^{2+}/CaM/channel complex may activate CDI mode (asterisk and black color indicate CDI activation, on-rate k_2 and off-rate k_{-2}).
doi:10.1371/journal.pcbi.1002061.g001

Transient Outward K^+ Current (I_{to})

The model for I_{to} was formulated based on newly measured experimental data. The measurements were from isolated undiseased human ventricular myocytes at 37°C (Figure 2A, white circles), and were carried out with the addition of 1 μM nisoldipine to the standard bath solution (see Methods) to block I_{CaL}. The holding potential was −90 mV. Currents were activated by a 300 ms step to various potentials. Inactivation time constants were determined from exponential fits to decay of these traces. To measure steady state inactivation, 500 ms steps from −90 mV to various potentials were followed by test pulses to 50 mV. Recovery from inactivation was determined at −90 mV, using P1/P2 pulses of 200 ms to 50 mV at varying interpulse intervals in a double pulse protocol.

The time constant for activation was determined by fitting time to peak from a digitized current trace (Amos et al.[22], their Figure 12C, in undiseased human ventricle at 37°C; $\tau_a = 2.645$ ms at $V_m = +40$ mV). Greenstein et al.[23] showed time to peak for hKv4.3 expressed in mouse fibroblast cells. The model provides a qualitative match to these data (considering temperature and expression system differences). That is, the model activation time constant decreases from a peak value of 6.5 to 1.5 ms in near linear fashion with increasing voltage from −20 to 60 mV.

The inactivation gate has two time constants, each with voltage dependent weighting. Inactivation kinetics and the I–V curve are accurate to the experimental data. A small divergence between simulations and experiments was observed at hyperpolarized potentials along the I–V curve (simulated current was less than in experiments). This may be due to the fact that experimentally measured currents were small and difficult to measure at these potentials. In fact, current was not measureable in 21, 11, 5, and 1 out of 23 cells at $V_m = -40$, −30, −20, and −10 mV, respectively. Currents with zero values were not included in the experimental I–V averages. However, these currents were included in averages for obtaining steady state activation and steady state inactivation curves in the model. This prevented over representation of the window current (small, appearing late during phase-3 of the AP, shown later). The conductance of the I_{to} model was set so that phase-1 behavior of the simulated AP would be similar to undiseased human endocardium experiments (small in endocardium; maximum value ~1 μA/μF). Measured endocardial APs showed rapid phase-1 repolarization, but did not show positive time derivatives during phase-1 (true notching was generally not observed). Thus, model I_{to} conductance was set to the maximum level which did not violate these observations (~1 μA/μF peak current at 1 Hz pacing).

CaMK effects on I_{to} were incorporated based on measurements by Tessier et al.[24] and Wagner et al.[25]. As in Tessier et al., CaMK shifted the voltage dependence of steady state activation 10 mV in the depolarization direction, and the time constant for development of inactivation was increased (multiplicative factor fit to match the voltage dependent increase). Wagner et al. showed that the time constant for recovery from inactivation was affected by CaMK (~2 fold faster).

Na^+/Ca^{2+} Exchange Current (I_{NaCa})

The I_{NaCa} model was formulated using measurements from undiseased human ventricular myocytes at 37°C (Figure 2B, white circles). The model was based on the framework established by Kang and Hilgemann[26], which allows for unlikely occurrence of inward Na^+ leak, without Ca^{2+} exchange. The Hilgemann model shows Na^+:Ca^{2+} exchange stoichiometry slightly greater than 3.0, as has been observed by others[27,28]. Though the Hilgemann model is mechanistically novel in this way, it can still reproduce all Na^+, Ca^{2+} and voltage dependent properties observed by Weber et al.[29] in the nonfailing human ventricle. Compare Hilgemann and Weber data to our simulated reproductions in Supplement Figures S1, S2 and S3 in Text S1. As in the Faber-Rudy[30] and Hund-Decker-Rudy models[19,31], we included 20% of the exchanger in the Ca^{2+} diffusion subspace[32,33]. The choice to include 20% in the subspace in human is validated based on its effect on the rate dependence of peak $[Ca^{2+}]_i$ (results in Supplement Figure S17 in Text S1). Values above or below 20% disrupt the demonstrated correspondence of peak $[Ca^{2+}]_i$ rate dependence with experiments (see section on Na^+ and Ca^{2+} rate dependence).

Inward Rectifier K^+ Current (I_{K1})

The model for I_{K1} was constructed based primarily on new experimental data, measured at 37°C in undiseased isolated human ventricular myocytes as the 0.5 mM $BaCl_2$ sensitive current (Figure 2C, white circles). Current was elicited with steps from −90 mV to various potentials for 300 ms. The current that remained at the end of the steps was recorded as I_{K1}.

Two gates were used in the model: R_{K1}, the instantaneous rectification gate, and x_{K1}, the time dependent inactivation gate. Importantly, previous models[9,10,34,35] have ignored both inactivation gating, and detailed $[K^+]_o$-dependence of I_{K1} (exception, I_{K1} equations by Fink et al.[36]). There are nonfailing human ventricular measurements which we utilized to include these effects[37,38].

Steady state rectification was determined by dividing current by driving force, then normalizing. Rectification was shown to be $[K^+]_o$-dependent in the nonfailing human ventricle by Bailly et al.[37]. A linear shift in $V_{1/2}$ for rectification toward more depolarized potentials with elevated $[K^+]_o$ was incorporated, as was shown experimentally (compare to Bailly et al., their

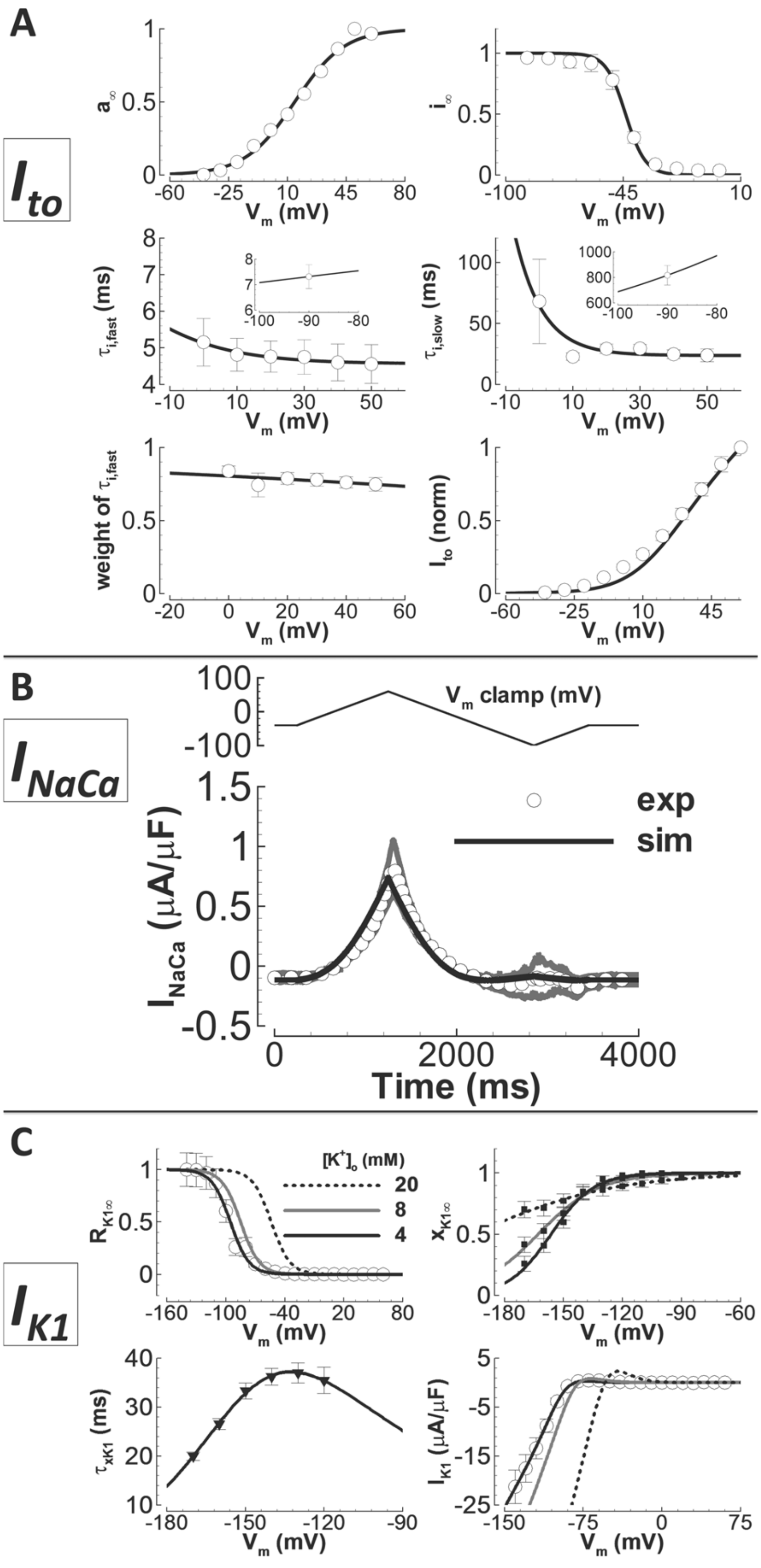
A
I_to
a∞
i∞
V_m (mV)
τ_i,fast (ms)
τ_i,slow (ms)
weight of τ_i,fast
I_to (norm)
B
I_NaCa
V_m clamp (mV)
I_NaCa (μA/μF)
exp
sim
Time (ms)
C
I_K1
[K+]_o (mM)
20
8
4
R_K1∞
x_K1∞
τ_xK1 (ms)
I_K1 (μA/μF)

Figure 2. Undiseased human I_{to}, I_{NaCa}, and I_{K1} experiments and model validation. A) I_{to}. Experimental data are white circles (N = 8 from 5 hearts for inactivation time constants, N = 10 from 5 hearts for recovery time constants, N = 9 from 6 hearts for steady state inactivation, and N = 23 from 8 hearts for the I–V curve). Simulation results are solid lines. From left to right, top to bottom: steady state activation, steady state inactivation, fast time constant for inactivation, slow time constant for inactivation (insets show fast and slow recovery from inactivation), relative weight of the fast component for inactivation and the I–V curve (normalized). B) I_{NaCa}. Experimental data are digitally averaged time traces (N = 3 from 2 hearts, white circles, gray is standard error of the mean). Simulation results are the solid line. Top) Voltage clamp protocol. Bottom) I_{NaCa} in response to the clamp. C) I_{K1}. Experimental data are previously unpublished (white circles, N = 21 from 12 hearts), from Bailly et al.[37] (black squares) and Konarzewska et al.[38](black triangles). Simulation results are solid lines (black, gray and dashed black for $[K^+]_o$ = 4, 8 and 20 mM). Top left) Voltage and $[K^+]_o$ dependence of steady state rectification. Top right) Voltage and $[K^+]_o$ dependence of steady state inactivation. Bottom left) Time constant for inactivation. Bottom right) I–V curve, and its $[K^+]_o$ dependence.
doi:10.1371/journal.pcbi.1002061.g002

Figure 4B). Bailly also showed the voltage and $[K^+]_o$-dependence of inactivation. We introduced the time dependent x_{K1} gate, based on these data. As was shown experimentally, both $V_{1/2}$ and the slope factor for inactivation depend linearly on $[K^+]_o$. The time constant for inactivation was based on measurements in nonfailing human ventricular myocytes by Konarzewska et al.[38] (their Figure 1C). Conductance was observed to be in proportion to the square root of $[K^+]_o$ in the human ventricle[37]. When assembled, the I_{K1} model demonstrated correspondence with the measured amplitude and rectification profile, and with Bailly data for $[K^+]_o$-dependence. As in Jost et al.[39], I_{K1} was voltage dependent, but not pacing rate dependent (Supplement Figure S4 in Text S1).

Rapid Delayed Rectifier K$^+$ Current (I_{Kr})

The model for I_{Kr} was constructed using experimental data measured in isolated undiseased human ventricular myocytes at 37°C (Figure 3A, white circles). Measurements were carried out with/without addition of 1 μM E-4031 to the standard bath solution in order to obtain the difference current. Tail currents were elicited by stepping from −40 mV to various potentials for 1000 ms, and then stepping back down to −40 mV. The deactivation time constant was determined by fitting the tail current decay. The time constant for activation was found by stepping from −40 mV to various potentials for various durations preceding a step back to −40 mV. The rate with which the envelope of tail currents developed at different voltages was measured with an exponential fit to obtain the time constant for activation. Since this process was well fit by a single exponential, we made the fast and slow time constants in the model converge on the activation limb, at depolarized potentials. The steady state activation curve was determined from the I–V curve, after dividing by the driving force, assuming maximal activation at the time of peak tail current. Slow deactivation of I_{Kr} (experiments and simulations, Figure 3B), suggests its participation in AP shortening during steady state pacing at fast rate and at short diastolic intervals during restitution; this hypothesis will be explored in a later section. The fast inactivation (rectification, instantaneous in the model) R_{Kr} gate was determined so that current profile matched experiments using a human AP voltage clamp (Figure 3C). Important features of the experimental AP clamp trace that the model reproduced include 1) the early recovery phase, where approximately half maximal current appeared by the beginning of the AP plateau, followed by 2) quasi-linear current increase until peak current was reached during late phase-3 of the AP.

Since enzymes used to disaggregate myocytes can significantly degrade I_{Kr}[40], conductance was scaled to provide correct APD90 in control and with I_{Kr} block, measured in small tissue preparations. Indeed, APD90 was a function of I_{Kr} conductance (parameter sensitivity, Supplement Figure S15 in Text S1). As in undiseased human ventricle experiments[39], I_{Kr} was voltage dependent, but not pacing rate dependent (Supplement Figure S5 in Text S1).

Slow Delayed Rectifier K$^+$ Current (I_{Ks})

Data from Virág et al.[41], measured in isolated undiseased human ventricular myocytes at 37°C, were used to construct the model for I_{Ks} (Figure 3D). The model has two gates: x_{s1} and x_{s2}. The x_{s1} gate is responsible for activation. Deactivation was controlled by x_{s2}. Activation/deactivation separation was based on the fact that activation was much slower than deactivation. Setting $\tau_{x1} >> \tau_{x2}$ at hyperpolarized potentials, where deactivation dominated, and $\tau_{x2} << \tau_{x1}$ at depolarized potentials, where activation dominated, allowed for separation of these processes as two gates. As in the case of I_{Kr}, it is understood that I_{Ks} is damaged (reduced) by enzymatic disaggregation of myocytes[42]. Therefore, we used I_{Ks} specific drug block (1 μM HMR-1556) effects on APD90, measured in small tissue preparations, to determine the correct conductance. Ca^{2+} dependence of I_{Ks} was incorporated based on measurements by Tohse et al.[43]. The effect of this dependence was negligible under physiological Ca^{2+} concentration conditions.

Fast Na$^+$ Current

Fast I_{Na} was formulated using nonfailing human ventricular data from Sakakibara et al.[44] (Figure 4A). Since Sakakibara experiments were performed at 17°C, a temperature adjustment was used to obtain the final model equations, representing behavior at 37°C. The effect of temperature on steady state gating was shown by Nagatomo et al.[45]. For activation, $V_{1/2}$ shift with temperature change from 23 to 33°C was +4.3 mV. For inactivation, the shift was +4.7 mV. We shifted $V_{1/2}$ by twice these amounts, assuming linearity (adjust to 37°C from data taken at 17°C, a change of 20°C; Nagatomo showed a change of 10°C). Time constants were adjusted to 37°C using Q_{10}. We set $Q_{10} = 2$ since Q_{10} was given as "about two" by Nagatomo.

Hanck and Sheets[46] documented a shift in $V_{1/2}$ with the passage of time after patch clamp commencement. For activation, the shift was −0.47 mV/min. It was −0.41 mV/min for inactivation. Sakakibara reported the time elapsed between patching and measurement for steady state activation and inactivation as between 10 and 20 min, ~15 min for both. Thus, we reversed the time dependent shifts in $V_{1/2}$.

CaMK effects on I_{Na} were based on available data[47]. We took into account the measured −6.2 mV $V_{1/2}$ shift in steady state inactivation, the roughly 3-fold slowing of current decay, and the 1.46-fold slowing of recovery from inactivation.

The non-temperature adjusted model I–V curve matches Sakakibara data at 17°C. We determined appropriate channel conductance at 37°C based on conduction velocity, and maximum dV_m/dt. Conduction velocity in a one dimensional fiber simulation was 45 cm/s during 1 Hz pacing, consistent with available (dog) experiments[48]. It was 70 cm/s when stimulated from quiescence, consistent with *in vivo* measurements in nonfailing human hearts[49]. Maximum dV_m/dt was 254 mV/ms in single cells at 1 Hz pacing, consistent with measurements from nonfailing human ventricular myocytes at 37°C (234±28 mV/ms)[50].

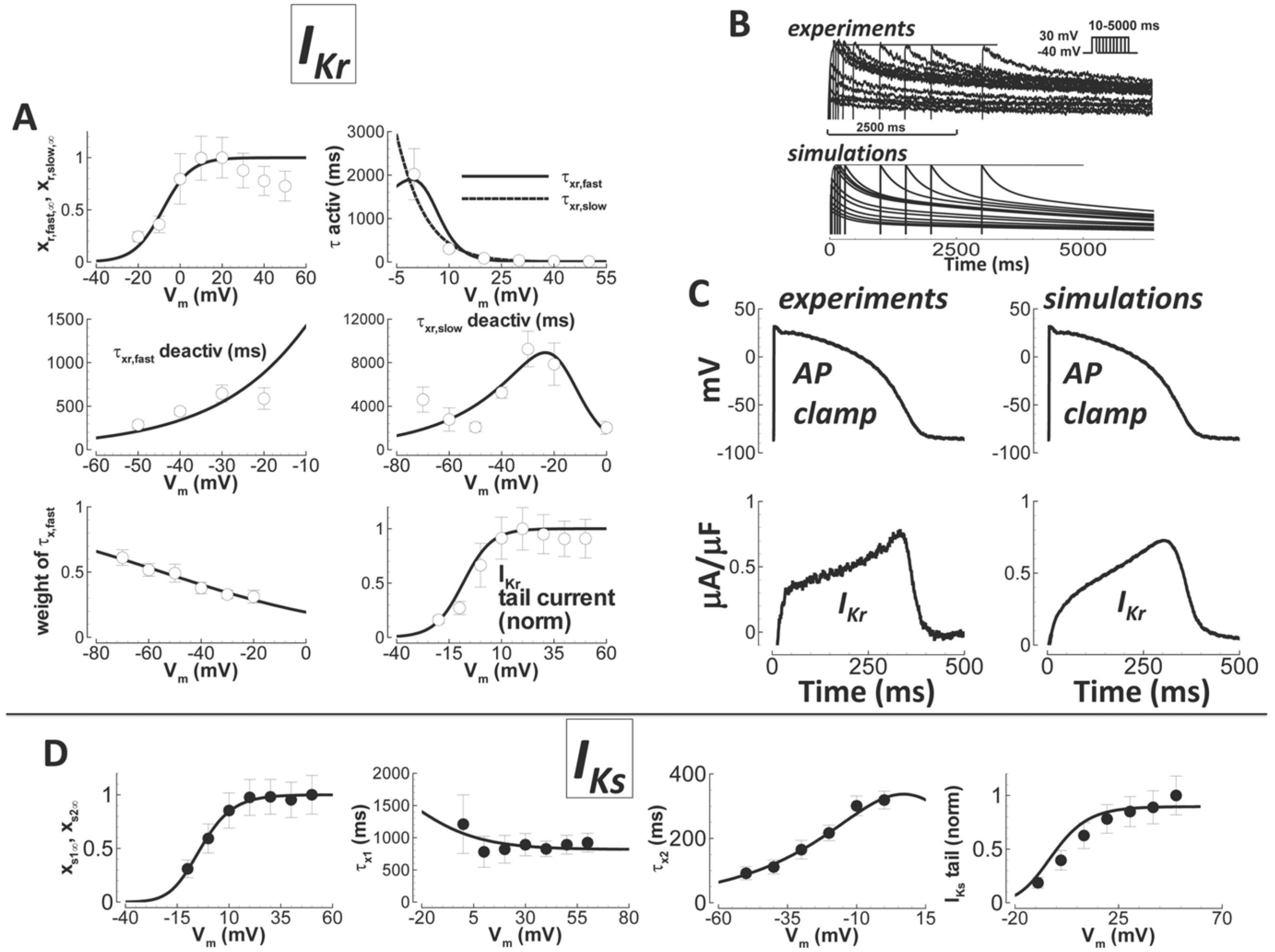

Figure 3. Undiseased human I_{Kr} and I_{Ks} experiments and model validation. A) I_{Kr}. Experimental data are white circles (N = 10 from 7 hearts for steady state activation, N = 7 from 3 hearts for activation and from 2 hearts for deactivation time constants and weights, and N = 10 from 7 hearts for tail currents). Simulation results are lines. From left to right, top to bottom: steady state activation, time constant for activation (fast (solid) and slow (dashed) time constants converge), fast time constant for deactivation, slow time constant for deactivation, relative weight of the fast component for deactivation, and the I–V curve for normalized tail currents. B) Activation/deactivation profiles in response to the voltage steps shown (−40 mV holding potential to +30 mV steps of various duration, followed by a return to −40 mV, top right inset). Experiments are above. Simulations are below. Activation is rapid, occurring within tens of milliseconds. Deactivation is slow, occurring after several seconds. C) Human AP clamp waveform (top), used to elicit 1 μM E-4031 sensitive current (I_{Kr}, bottom); experiments are on the left, and comparison to simulations using the same AP clamp is on the right. D) I_{Ks}. Data are from Virág et al.[41] (black circles). Simulation results are solid lines. From left to right: steady state activation, time constant for activation (much slower than deactivation at depolarized potentials), time constant for deactivation (much faster than activation at hyperpolarized potentials), and the I–V curve, showing normalized tail currents.

doi:10.1371/journal.pcbi.1002061.g003

Late Na^+ Current

Data used in the formulation of late I_{Na} were from Maltsev et al.[51], measured in the nonfailing human ventricle (Figure 4B), functionally defined in experiments and simulations as the Na^+ current remaining after 200 ms from the onset of depolarization. Steady state activation was derived from the I–V curve (current divided by driving force, then normalized). The time constant for activation of late I_{Na} was identical to that for fast I_{Na}. It is not possible to measure the time to peak for late I_{Na} because of the interfering effects of the much larger I_{Na}. However, in the model scheme, the measurement is irrelevant for the same reason.

The h_L gate is responsible for both development of and recovery from inactivation. The time constant for development was adjusted using $Q_{10} = 2.2$, as measured by Maltsev et al.[52] (hNav1.5 channels expressed heterologously). The time constant was voltage independent[51]. Maltsev et al.[51] reported a maximum late I_{Na} of -0.356 pA/pF in nonfailing human ventricular myocytes (average current between 200 and 220 ms during step to -30 mV from -120 mV, their Table 2, donor heart average). We scaled the Maltsev I–V curve to the donor value and used it to determine the model conductance.

We do not consider fast and late Na^+ currents to be separate channels. Rather, they have long been understood to represent different gating modes (experiments[52], and simulations by our group[53]), separated functionally in time. In experiments, and in simulated reproductions of experiments, late I_{Na} was functionally defined as the I_{Na} current persisting 200 ms after onset of depolarization. CaMK dependence was implemented (-6.2 mV $V_{1/2}$ shift in steady state inactivation, and 3-fold slowing of inactivation time constant, as measured[47]).

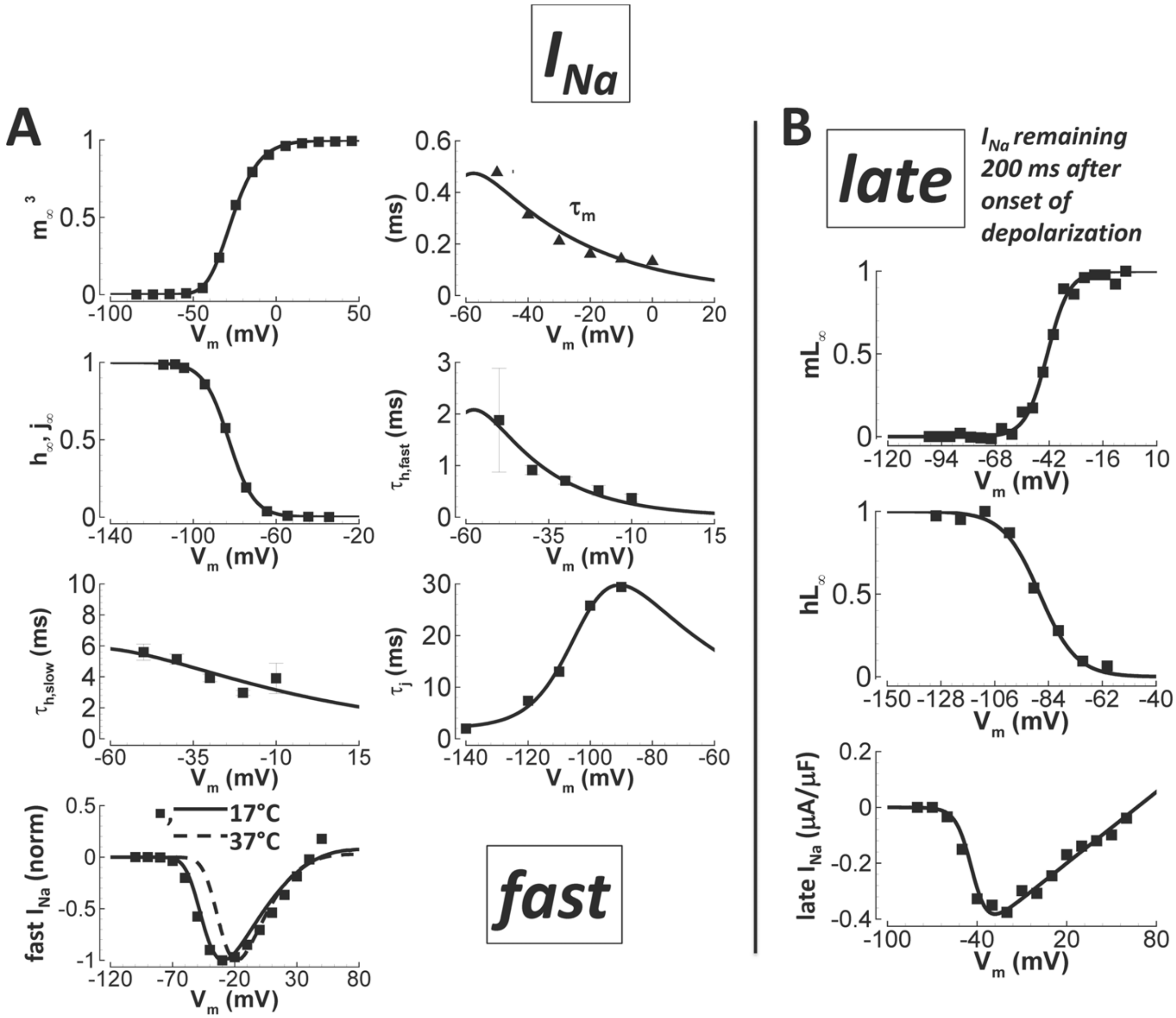

Figure 4. Nonfailing human fast I_{Na} and late I_{Na} experiments and model validation. A) Fast I_{Na}. Experiments are from Sakakibara et al.[44] (black squares) and Nagatomo et al.[45] (black triangles). Simulation results are solid lines. From left to right, top to bottom: steady state activation, time to peak (experiment) and activation time constant (simulation), steady state inactivation, fast time constant for development of inactivation, slow time constant for development of inactivation, time constant for recovery from inactivation, and the I–V curve (solid line simulation and data at 17°C, dashed line simulation at 37°C). In other panels, simulations and data were adjusted to 37°C. Time to peak was fit at 33°C. B) Late I_{Na}. Experiments are from Maltsev et al.[51] (black squares). Simulation results are solid lines. Top) Steady state activation. Middle) Steady state inactivation. Bottom) I–V curve.
doi:10.1371/journal.pcbi.1002061.g004

Na^+/K^+ ATPase Current (I_{NaK})

The model for I_{NaK} was reformulated based on the work of Smith and Crampin[54]. The Smith and Crampin model includes more detail than standard formulations employed by other ventricular AP models[9,10,34,35]. Importantly, the Smith and Crampin framework includes $[K^+]_i$ dependence and inputs for ATP and pH sensitivity. Here, we set ATP and pH values to normal physiological levels (pH was dynamic when stated). Dynamically changing $[K^+]_i$ is a known and meaningful pump regulator that is a functioning part of this model. High $[K^+]_i$ (combined with low ATP) can make the pump reverse, bringing Na^+ in, as has been observed in isolated hearts[55].

The Smith and Crampin model (schematized in Supplement Figure S6 in Text S1) was adjusted to reproduce the basic findings of Nakao and Gadsby[56], demonstrating $[Na^+]_o$ dependence, $[Na^+]_i$ dependence with high and low $[Na^+]_o$, and $[K^+]_o$ dependence with high and low $[Na^+]_o$ (Supplement Figure S7 in Text S1). To determine human ventricle appropriate conductance for I_{NaK}, we used $[Na^+]_i$-frequency data presented by Pieske et al.[57] as a target (nonfailing human left ventricular myocytes at 37°C).

The I_{NaK} formulation is based on known biophysical properties[54]; its behavior reproduces available experimental observations[56] (Supplement Figure S7 in Text S1). However, no direct measurement of I_{NaK} has been made in the nonfailing or undiseased human ventricle. To endow human ventricle specificity to I_{NaK}, our strategy was indirect; reproducing the rate dependence of intracellular Na^+ concentration, $[Na^+]_i$, measured in the nonfailing human ventricle was the target. This choice

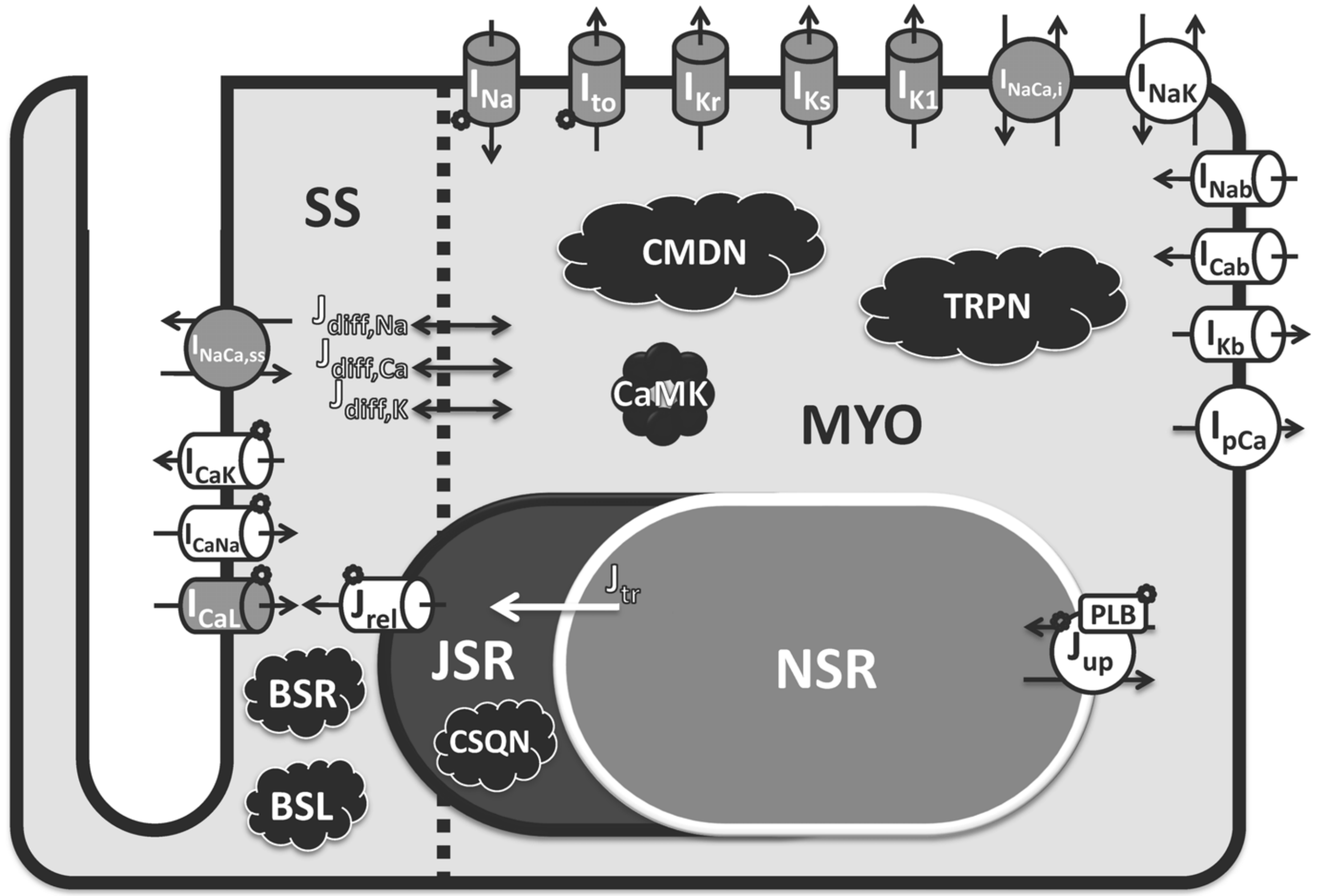

Figure 5. Schematic diagram of human ventricular myocyte model. Formulations for all currents and fluxes were based either directly (gray) or indirectly (white) on undiseased or nonfailing human experimental data. Model includes four compartments: 1) bulk myoplasm (myo), 2) junctional sarcoplasmic reticulum (JSR), 3) network sarcoplasmic reticulum (NSR), and 4) subspace (SS), representing the space near the T-tubules. Currents into the myoplasm: Na^+ current (I_{Na}; representing both fast and late components), transient outward K^+ current (I_{to}), rapid delayed rectifier K^+ current (I_{Kr}), slow delayed rectifier K^+ current (I_{Ks}), inward rectifier K^+ current (I_{K1}), 80% of Na^+/Ca^{2+} exchange current ($I_{NaCa,i}$), Na^+/K^+ pump current (I_{NaK}), background currents (I_{Nab}, I_{Cab}, and I_{Kb}), and sarcolemmal Ca^{2+} pump current (I_{pCa}). Currents into subspace: L-type Ca^{2+} current (I_{CaL}, with Na^+ and K^+ components I_{CaNa}, I_{CaK}), and 20% of Na^+/Ca^{2+} exchange current ($I_{NaCa,ss}$). Ionic fluxes: Ca^{2+} through ryanodine receptor (J_{rel}), NSR to JSR Ca^{2+} translocation (J_{tr}), Ca^{2+} uptake into NSR via SERCA2a/PLB (J_{up}; PLB - phospholamban), diffusion fluxes from subspace to myoplasm ($J_{diff,Na}$, $J_{diff,Ca}$, and $J_{diff,K}$). Ca^{2+} Buffers: calmodulin (CMDN), troponin (TRPN), calsequestrin (CSQN), anionic SR binding sites for Ca^{2+} (BSR), anionic sarcolemmal binding sites for Ca^{2+} (BSL). Ca^{2+}/calmodulin-dependent protein kinase II (CaMK) and its targets are labeled.
doi:10.1371/journal.pcbi.1002061.g005

assumes that the major role for I_{NaK} is maintenance of physiological $[Na^+]_i$. In the model, $[Na^+]_i$ and its relative changes with pacing rate are controlled by I_{NaK} conductance (~0.5 mM change per 20% change in I_{NaK} conductance, Supplement Figure S18 in Text S1). In the absence of direct human ventricle I_{NaK} measurements, validation of the I_{NaK} formulation employs this relationship.

Human AP Characteristics and APD

Figure 5 shows a schematic diagram of the human ventricular AP model. The scheme was largely unchanged from the recent dog ventricular model by Decker et al.[19]. However, additional targets for CaMK were included, as described above, based on new findings. Currents were reformulated based on new undiseased or published nonfailing human experiments. These are colored gray in Figure 5. Currents and fluxes colored white in the figure were based on human specific measurements of rate dependence of intracellular Na^+ and Ca^{2+} concentrations ($[Na^+]_i$ and $[Ca^{2+}]_i$, respectively), which these currents/fluxes affect. Equations for currents and fluxes were not adopted from other human or animal models without substantive modification; all equations were reformulated with the exceptions of Ca^{2+} buffers, CaMK kinetics, and background currents, for which we used Decker et al.[19] formulations and adjusted conductances. Model equations for all major currents were completely reformulated (i.e. fast I_{Na}, late I_{Na}, I_{to}, I_{CaL}, I_{Kr}, I_{Ks}, I_{K1}, I_{NaCa}, and I_{NaK}). Relevant details precede equations in Supplement Text S1.

Microelectrode AP recordings from undiseased human ventricular endocardium at 37°C were used to validate basic human model AP characteristics. Figure 6A shows simulated APs and experimentally measured example APs for comparison during steady state pacing at the cycle lengths (CLs) indicated. We also compared simulated values for resting voltage, maximum voltage, and the maximum upstroke velocity, dV_m/dt, with experiments (Figure 6B). These comparisons were made for a single beat, stimulated from the quiescent state.

For steady state rate dependence, we compared APD30–90 after pacing at different CLs (Figure 7A). For restitution, we

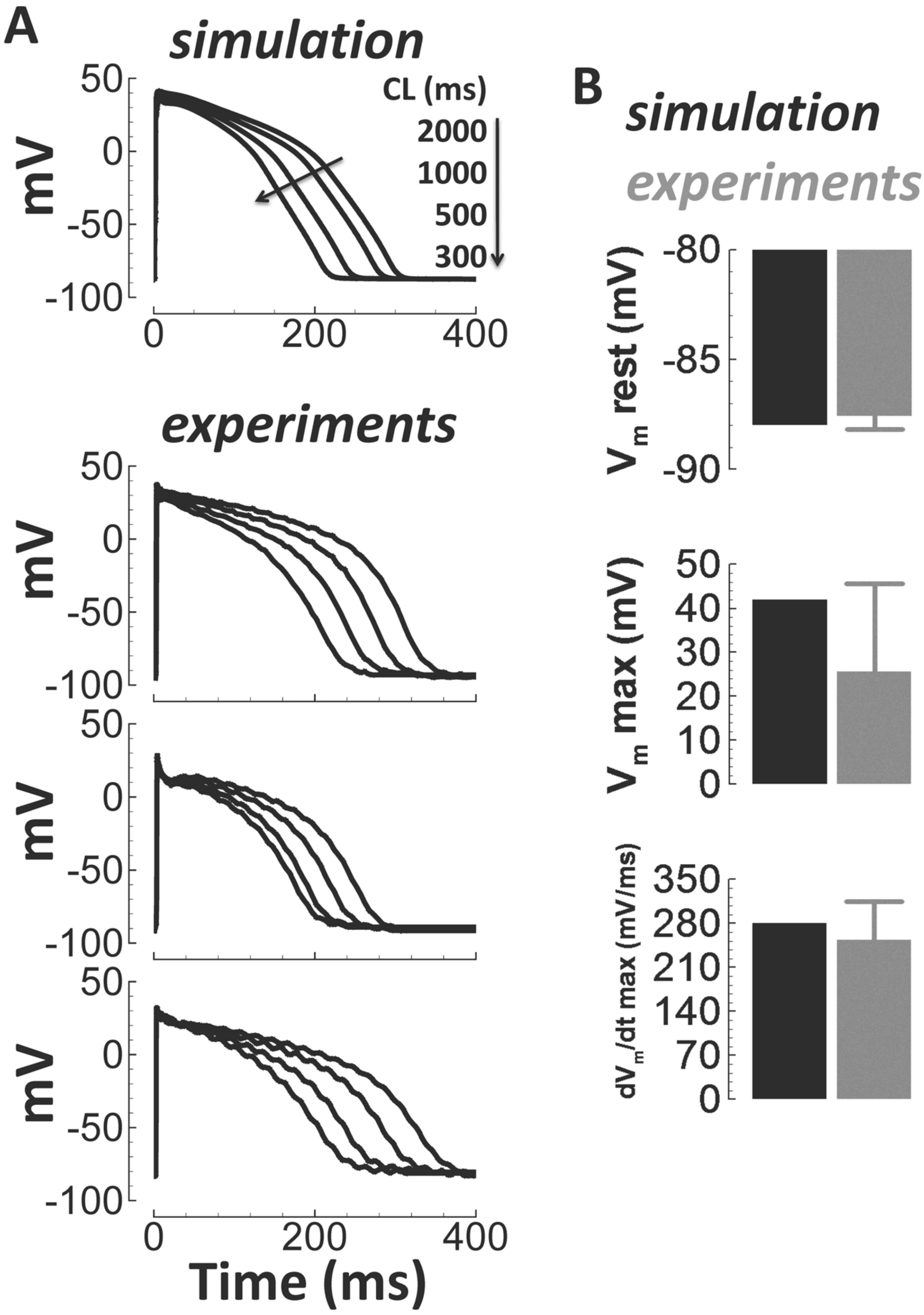
A
simulation
CL (ms)
2000
1000
500
300
mV
50
0
-50
-100
0
200
400
experiments
mV
50
0
-50
-100
mV
50
0
-50
-100
mV
50
0
-50
-100
0
200
400
Time (ms)
B
simulation
experiments
V_m rest (mV)
-80
-85
-90
V_m max (mV)
50
40
30
20
10
0
dV_m/dt max (mV/ms)
350
280
210
140
70
0

Figure 6. Undiseased human endocardial AP traces from experiments (small tissue preparations) and model simulations. Simulated APs for a range of pacing frequencies (top) and corresponding examples of experimentally recorded APs at 37°C (below). Arrows indicate cycle length (CL) changes. B) Comparison of simulation (black) and experimentally measured (gray, small tissue preparations) basic AP parameters for a single paced beat from quiescence (37°C, N = 32 from 32 hearts). Shown, from top to bottom, are the resting membrane potential (V_m rest), maximum upstroke potential (V_m max), and maximum upstroke velocity (dV_m/dt max).
doi:10.1371/journal.pcbi.1002061.g006

compared APD30–90 after steady state S1 pacing at CL = 1000 ms, followed by a single S2 extrasystolic stimulus delivered at various diastolic intervals (DIs, measured relative to APD90, Figure 7B). Model AP repolarization from 30 to 90% quantitatively reproduced this extensive dataset (simulation results were within experimental error bars). Generally, electrotonic effects of tissue coupling were minor (see Discussion and Supplement Figure S8 in Text S1).

The rate of repolarization in the model was gradual, as in experiments (APD30–90 were well separated in time, Figure 7C). Other models repolarized more rapidly and late compared to these experiments (simulations were all endocardial cell types).

Koller et al.[58] measured dynamic restitution in the nonfailing human ventricle with monophasic AP electrodes. Following the Koller protocol (explained in Methods), the human model matched Koller results (Figure 7D). Simulations predict a bifurcation (alternans) at shortest DIs (<90 ms), which is also observed in the experiments.

Steady state rate dependence and restitution of the undiseased human ventricular APD were also measured in the presence of channel-specific blockers (Figure 8, white squares, see Methods for further details). In Figure 8, drugs and applied doses are provided for each experiment. Simulated block was based on experimental dose-response measurements (E-4031[59], HMR-1556[60], nisoldipine[61], BaCl$_2$[62], ryanodine[63], and mexiletine[64], for block of I_{Kr}, I_{Ks}, I_{CaL}, I_{K1}, J_{rel}, and late I_{Na}, respectively). Simulations matched these experiments; that is, simulation results were within experimental error bars.

As pacing CL was decreased from 2000 to 300 ms, currents in the human ventricular AP model changed accordingly (Figure 9). Due to increased refractoriness at faster rates, maximum fast I_{Na}, late I_{Na}, and I_{to} were reduced. By contrast, peak I_{CaL} increased,

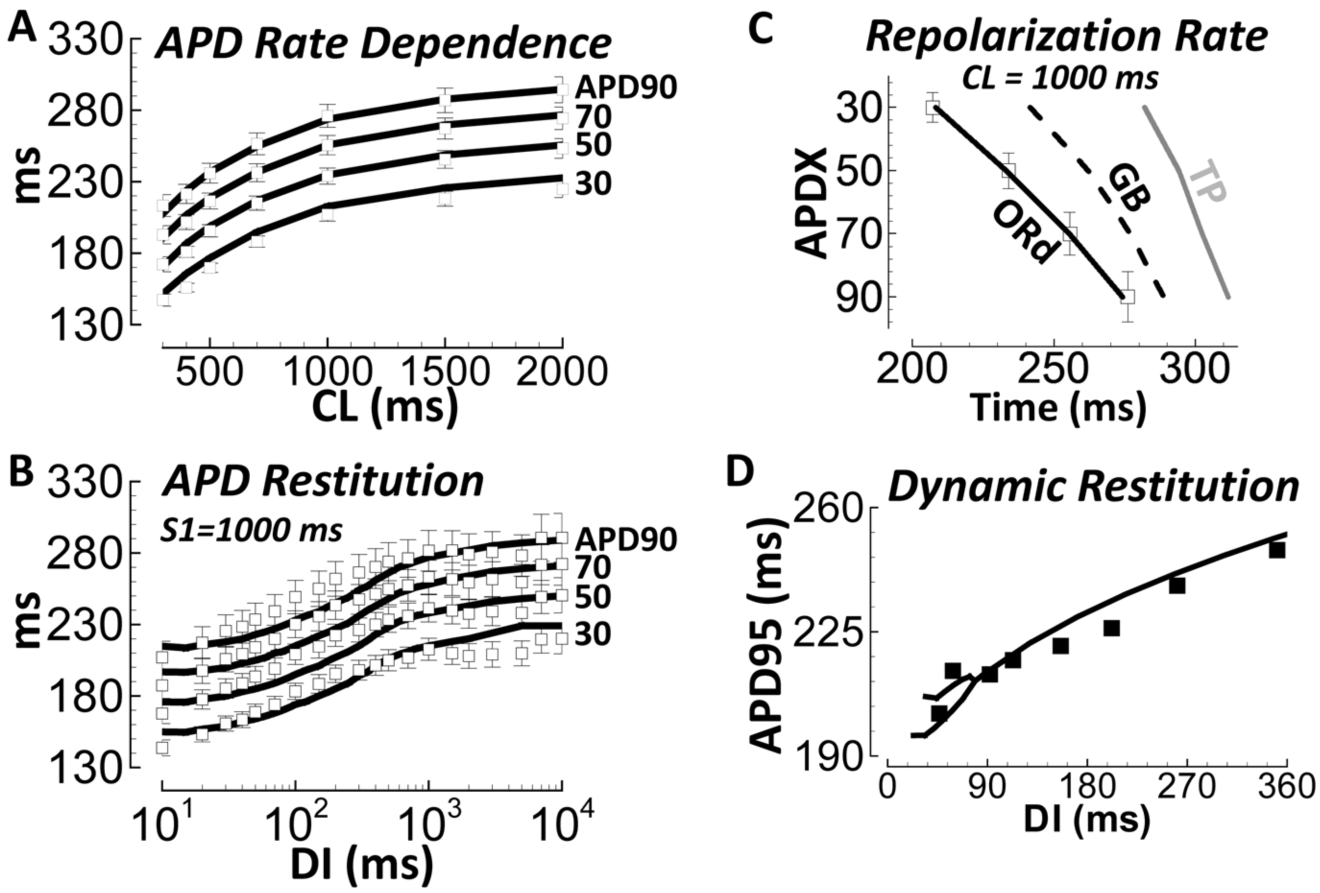

Figure 7. Undiseased human endocardial AP response to pacing protocols from experiments (small tissue preparations) and model simulations. A) Steady state APD rate dependence. B) S1S2 APD restitution (DI – diastolic interval). APD30–90 are labeled at right. Solid lines are simulation results; white squares are experiments at 37°C (N = 140 hearts in panel A, N = 50 hearts in panel B). C) Repolarization rate at CL = 1000 ms. Trajectory of APD30 to APD90 is accurate in the ORd model (white squares are experimental data); less so in other models. D) Dynamic restitution protocol (see Methods). Experiments are from Koller et al.[58], measured in nonfailing human hearts with monophasic AP electrodes (black squares). Simulated results are the black line. At very short diastolic intervals (DI<90 ms), the model shows APD bifurcation (alternans).
doi:10.1371/journal.pcbi.1002061.g007

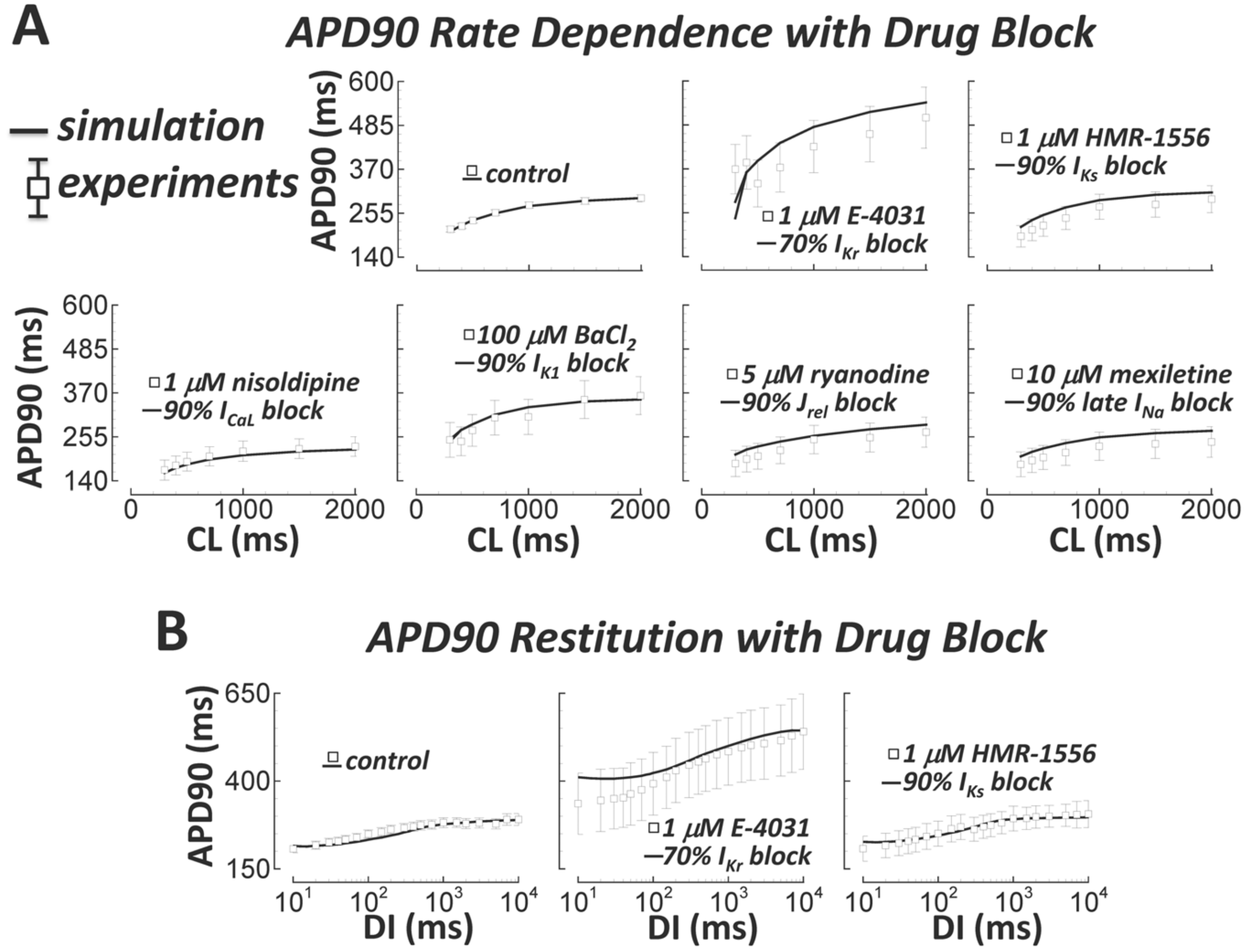

Figure 8. Pacing protocols with block of various currents. Experimental data (small tissue preparations) are white squares. A) Steady state APD90 rate dependence. From left to right, top to bottom: N = 140, 5, 5, 5, 5, 4, and 4 hearts. Shown are control, I_{Kr}, I_{Ks}, I_{CaL}, I_{K1}, RyR, and late I_{Na} block. B) APD90 restitution (S1 = 1000 ms). From left to right: N = 50, 3, and 4 hearts. Shown are control, I_{Kr}, and I_{Ks} block.
doi:10.1371/journal.pcbi.1002061.g008

due in part to CaMK-phosphorylation induced facilitation[65]. I_{Kr} and I_{K1} were largely rate independent. Mild I_{Ks} accumulation[66] caused rate dependent increase in current. I_{NaK} became larger due to intracellular Na^+ accumulation at fast pacing rates (details below). $I_{NaCa,i}$, and $I_{NaCa,ss}$ became more inward, in order to remove increasing Ca^{2+}.

Transmural Heterogeneity

Changes in mRNA and protein expression across the transmural wall using undiseased human ventricles were measured[67,68,69]. Functional data for transmural changes in I_{to} were measured in nonfailing human ventricular myocytes[70]. These results were compiled to create a complete dataset for transmural differences between endocardial (endo), mid-myocardial (M), and epicardial (epi) cell types. We considered transmural differences in Nav1.5, Cav1.2, HERG1, KvLQT1, Kir2.1, NCX1, Na/K ATPase, Kv1.5, RyR2, SERCA2, and CALM3 to be represented in the model by late I_{Na}, I_{CaL}, I_{Kr}, I_{Ks}, I_{K1}, I_{NaCa}, I_{NaK}, I_{Kb}, J_{rel}, J_{up}, and CMDN, respectively. Whenever an expression ratio was not available, we chose unity. Using this analysis, models for M and epi cells were derived from the thoroughly validated endo model (Figure 10A–10D; equations on page 19 in Supplement Text S1).

In Figure 10E1, our experimental measurements for endo APD90 were scaled by M/endo and epi/endo APD90 ratios measured by Drouin et al.[50] and compared to simulations. Drouin experiments did not show results for CL<1000 ms. Epi simulations seem to deviate from Drouin experiments at faster pacing rates. However, epi simulations were consistent with nonfailing human epi experimental measurements at fast pacing rates (CL <1000 ms) recorded using optical mapping by Glukhov et al.[71] (panel E2). The rate dependence of simulated AP morphology in the different cell types (Figure 10F) was similar to Drouin recordings[50]. Relative shape and duration of simulated transmural APs were also consistent with those recorded by Glukhov et al.[71] from the heart of a 20 year old healthy human male (Supplement Figure S9 in Text S1). The transmural repolarization gradient direction was such that the pseudo-ECG T-wave was upright and rate dependent[72] as expected (Figure 10G).

Early Afterdepolarization (EAD)

Experiments from Guo et al.[73] in isolated nonfailing human ventricular endo myocytes showed EADs when paced very slowly (CL = 4000 ms) in the presence of the I_{Kr} blocker dofetilide

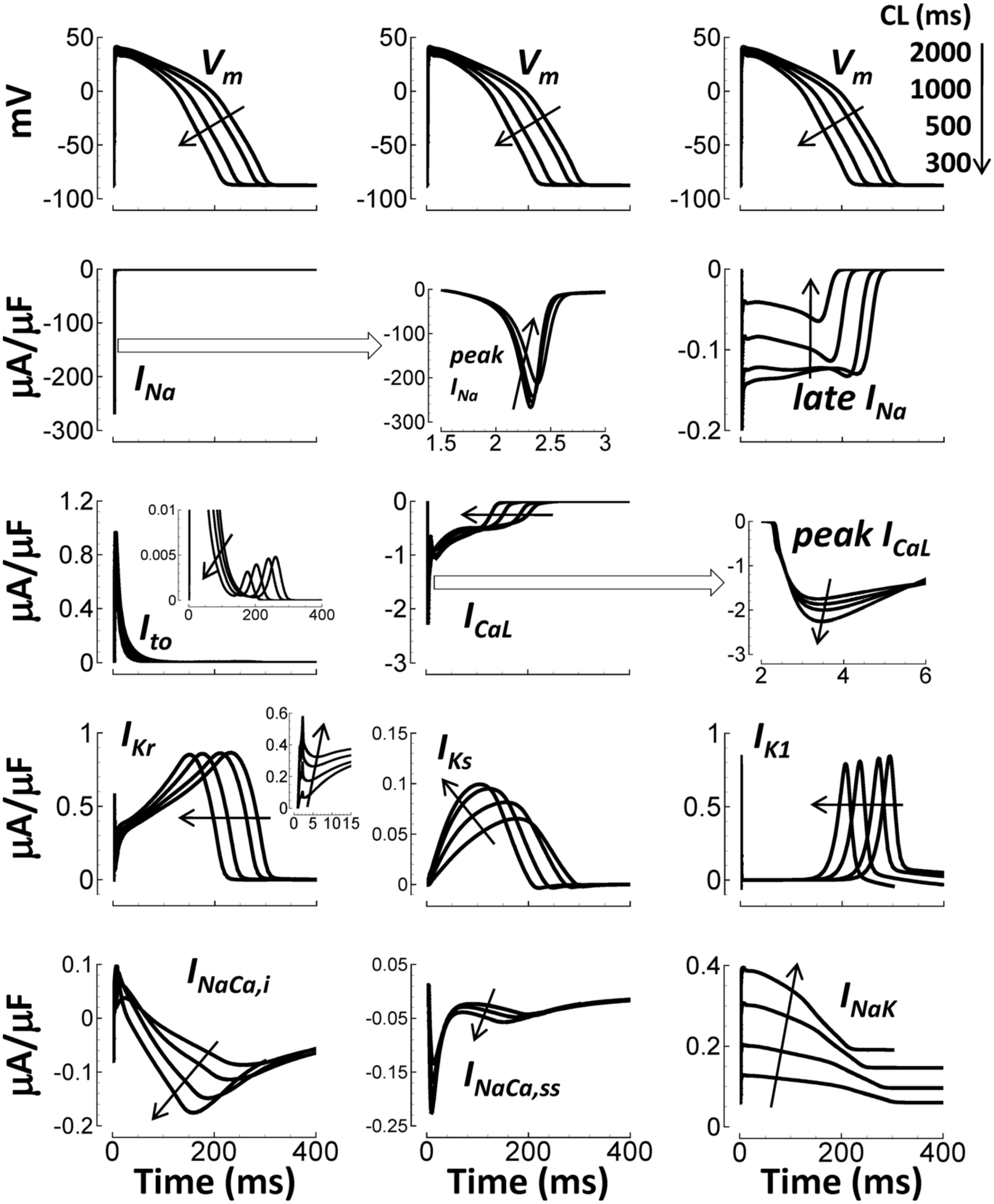

Figure 9. Rate dependence of currents at steady state. Black arrows indicate CL decrease (rate increase). Top Row) Simulated APs, repeated in each column for timing purposes. Lower Rows (left to right, top to bottom): I_{Na}, peak I_{Na} detailed time course, late I_{Na}, I_{to}, I_{CaL}, I_{CaL} increasing peaks with increasing pacing rate, I_{Kr}, I_{Ks}, I_{K1}, $I_{NaCa,i}$, $I_{NaCa,ss}$, and I_{NaK}. Insets show greater detail of late small I_{to} window current, and early I_{Kr} spiking at fast rates.

doi:10.1371/journal.pcbi.1002061.g009

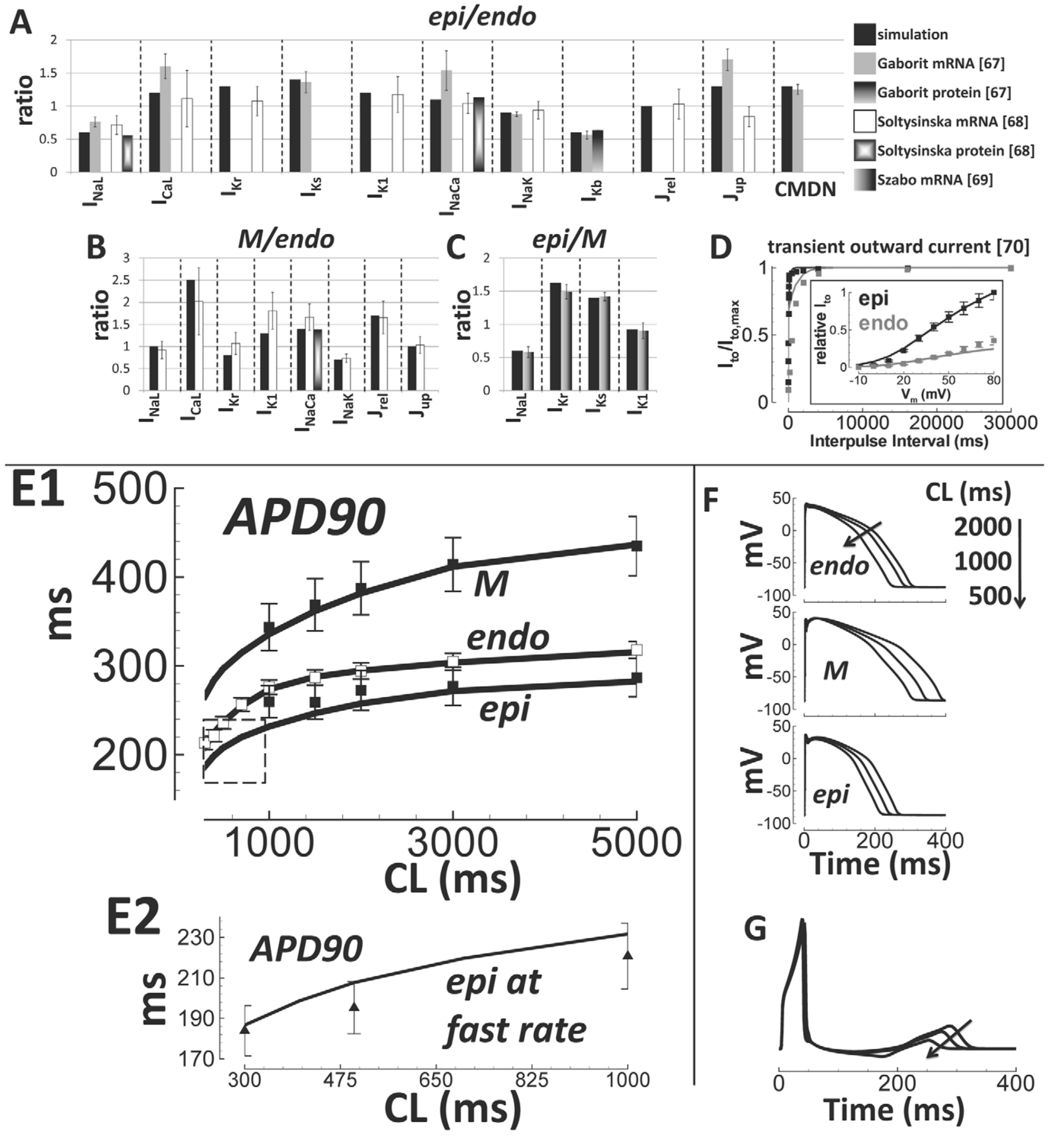

Figure 10. Transmural heterogeneity and validation of transmural cell type models. A–C) Expression ratio in the model (black bars) compared to experimental data from undiseased human hearts (grayscale bars, labeled). D) Transmural heterogeneity of I_{to}; simulations are lines, experiments are squares. Results for endo are gray; those for epi are black. E1) Rate dependence of APD90 in endo, M, and epi cell types. Epi and M data were obtained by scaling endo data (white squares) by epi/endo and M/endo APD90 ratios from Drouin et al.[50] (black squares). Simulations are black lines. E2) Same format as panel E1, showing epi APD90 at faster pacing rates. Data are from Glukhov et al.[71], (epi/endo scaling, black triangles). F) Top to bottom: Rate-dependence of endo, M, and epi APs. G) Pseudo-ECG, using a simulated transmural wedge. CL changes are indicated by arrows.

doi:10.1371/journal.pcbi.1002061.g010

(0.1 μM dose, ~85% I_{Kr} block[74]). In Figure 11A, we display Guo experimental results and simulation results of the same protocol using the ORd model, and the GB and TP models (all for endo cells at steady state). As in the experiment, the ORd model produced an EAD when paced at slow rate ($CL = 4000$ ms) with block of I_{Kr} (85%). Experiments and simulations both show a

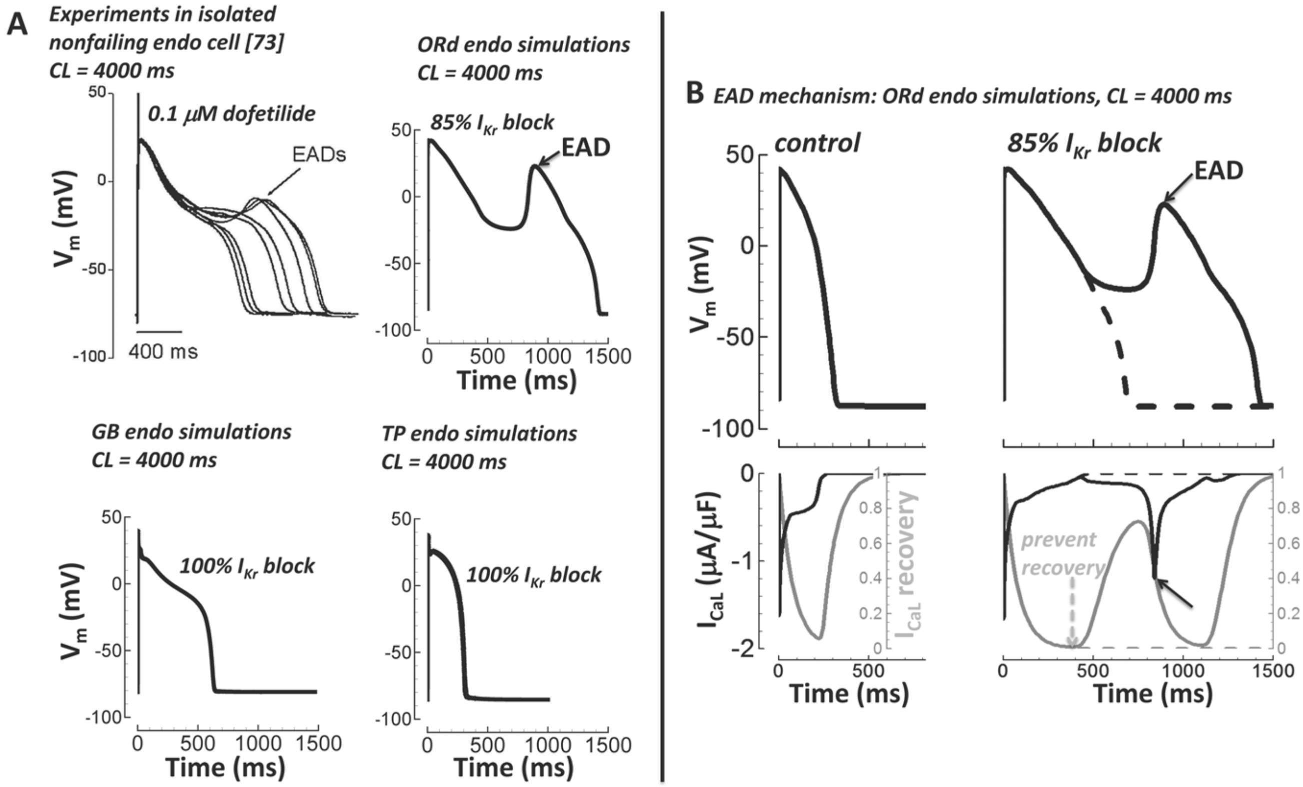

Figure 11. Early afterdepolarizations (EADs). A) Top left) Experiments in isolated nonfailing human endo myocytes from Guo et al.[73] showed EADs with slow pacing (CL = 4000 ms) in the presence of I_{Kr} block (0.1 μM dofetilide, ~85% I_{Kr} block[74], reproduce with permission). Top right) Following the experimental protocol of Guo et al. (CL = 4000 ms, 85% I_{Kr} block) the ORd model accurately showed a single large EAD. Bottom) GB (left) and TP (right) models failed to generate EADs (CL = 4000 ms, even with 100% I_{Kr} block). B) EAD mechanism. APs are on top. I_{CaL} (black) and I_{CaL} recovery gate (gray) are below. Slow pacing alone (CL = 4000 ms) did not cause an EAD (left). Slow pacing plus I_{Kr} block (85%) caused an EAD (solid lines, right). The EAD was depolarized by I_{CaL} reactivation during the slowly repolarizing AP plateau (solid lines, solid arrows). When I_{CaL} recovery was prevented, the EAD was eliminated (dashed lines and dashed arrow).
doi:10.1371/journal.pcbi.1002061.g011

single, large EAD deflection. The GB and TP models failed to produce an EAD following the same protocol (CL = 4000 ms), even with complete block of I_{Kr} (100%).

EADs in the ORd model were caused by I_{Kr} block induced prolongation of the time at plateau voltages, allowing I_{CaL} reactivation. When I_{CaL} recovery was prevented, the EAD was eliminated (inactivation gate clamping protocol, Figure 11B). This mechanism is the same as shown previously in other species[75].

Na^+ and Ca^{2+} Rate Dependence

Using data from nonfailing human ventricle, we validated rate dependent changes in concentrations of intracellular Na^+ and Ca^{2+}. For $[Na^+]_i$ changes with pacing rate, we used data from Pieske et al.[57], measured in the nonfailing human ventricle, normalized to 0.25 Hz pacing rate (Figure 12A). Reproduction of this curve implied that I_{NaK} magnitude was accurate (I_{NaK} conductance controls intracellular Na^+, thus rate dependence of relative accumulation, Supplement Figure S18 in Text S1). For Ca^{2+}, we used data from Schmidt et al.[76], normalized to the value at 0.5 Hz pacing rate. A personal correspondence with senior author J. Gwathmey revealed that pacing in the experiments was for about 100 beats (long enough to reach apparent steady state). Following this protocol, we showed the reduction in peak Ca^{2+} observed at the fastest pacing rates (Figure 12B). However, at true steady state, peak Ca^{2+} increased monotonically with pacing rate (shown in Figure 13).

Using Fura-2-AM fluorescence data measured in an undiseased isolated human ventricular myocyte at 37°C, we determined that the ORd model showed accurate intracellular Ca^{2+} decay (Figure 12C and 12D). Time constant fits were a single exponential decay from time of peak Ca^{2+}. The decrease in decay time constant observed with increase in pacing rate is a measure of frequency dependent acceleration of relaxation, an important validation of Ca^{2+} cycling.

Ca^{2+} Cycling and CaMK

As pacing rate increased, so did the CaMK active fraction ($CaMK_{active}$, Figure 13A, validated previously[31,77]). CaMK was important for controlling rate dependence of Ca^{2+} cycling in the model. In the absence of CaMK: Ca^{2+} transient amplitude was reduced, diastolic Ca^{2+} was elevated, JSR Ca^{2+} content and evacuation were rate independent, and Ca^{2+} reuptake (J_{up}) and release (J_{rel}) were severely blunted (Figure 13B).

Alternans

Koller et al.[58] showed that in the nonfailing human ventricle (*in vivo* monophasic AP recordings), APD alternans appeared at CLs <300 ms (rates >200 bpm). The amplitude of APD alternans was ~10 ms. These findings were reproduced by the human

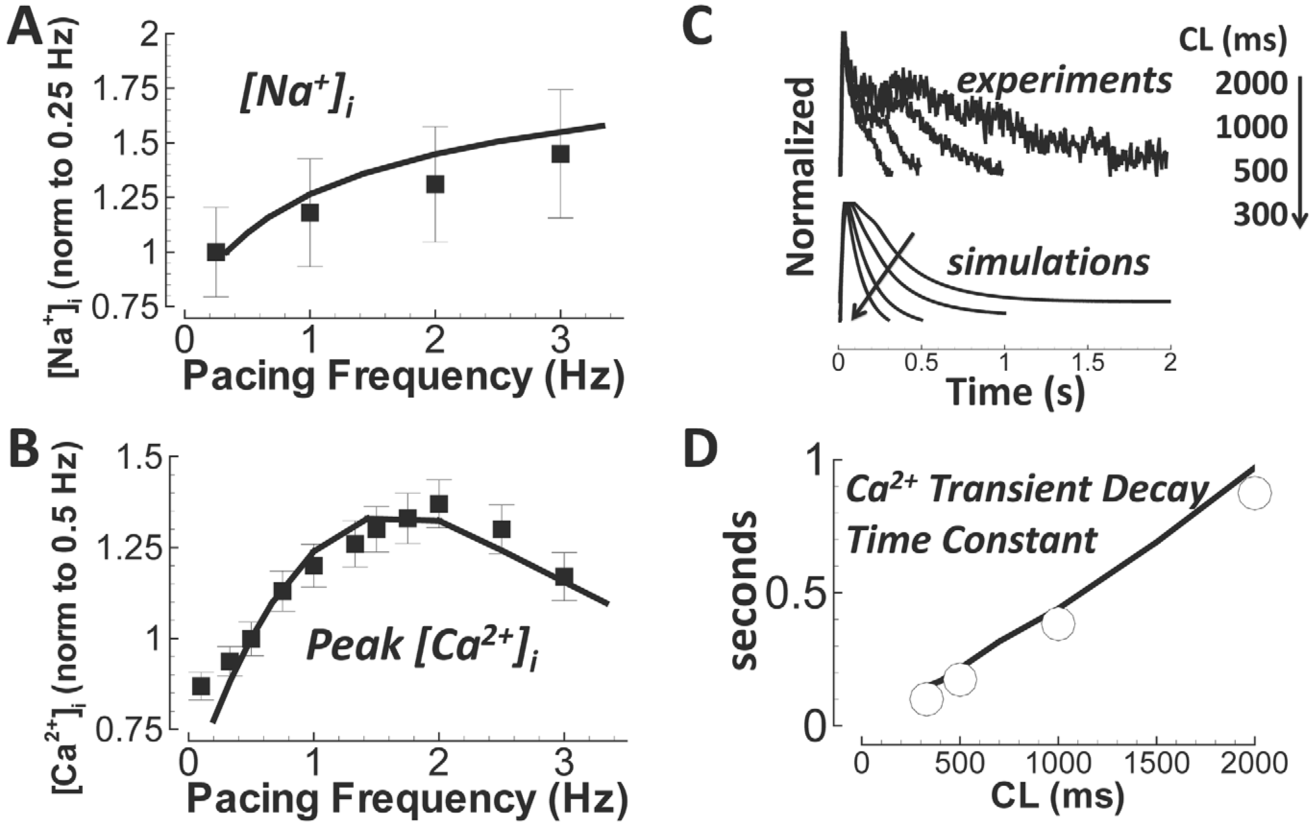

Figure 12. Rate dependence of intracellular ion concentrations. Simulation results are solid lines. A) [Na$^+$]$_i$ versus pacing frequency (normalized to 0.25 Hz). Experiments are from nonfailing myocytes (Pieske et al.[57], black squares). B) Peak Ca^{2+} transient (normalized to 0.5 Hz). Experiments are from nonfailing myocytes (Schmidt et al.[76], black squares). C) Ca^{2+} transients from experiments (Fura-2-AM) and simulations. Results are normalized to illustrate the time course of decay. The arrow indicates pacing CL changes. D) Frequency dependent acceleration of relaxation. Undiseased human experimental data are white circles. Simulations are the black line.
doi:10.1371/journal.pcbi.1002061.g012

model (APD alternans of 11 ms at CL = 250 ms, Figure 14). Pacing at rates faster than 230 ms in the model caused 2 to 1 block (i.e. failed APs every other beat), because APD began to encroach upon the pacing cycle length, leading to enhanced refractoriness of Na$^+$ current due to incomplete repolarization.

Since Koller measurements were performed in intact hearts, electrotonic coupling effects would have played a role. Therefore, simulations in a strand of 100 coupled endo cells were conducted to test whether alternans occurred in coupled tissue as well. Indeed, during CL = 280 ms steady state pacing, alternans developed in the multicellular fiber (results shown in Supplement Figure S10 in Text S1).

As in Livshitz et al.[77], beat to beat alternans in the Ca^{2+} subsystem were the cause of the APD alternans in the model. Longer APs coincided with larger Ca^{2+} transients. For steady state pacing at 250 ms pacing cycle length (shown in Figure 14A), we found that clamping the subspace Ca^{2+} concentration to either the odd or even beat waveforms eliminated alternans, but clamping of the voltage, myoplasmic Ca^{2+}, I_{CaL}, or I_{NaCa} did not eliminate alternans (odd or even beat clamp, not shown).

Cutler et al.[78] demonstrated that 30% SERCA upregulation eliminated alternans. Similarly, in our human model, a 20% increase in J_{up} magnitude eliminated alternans (shown in Supplement Figure S11 in Text S1). CaMK suppression also eliminated alternans in the model (Figure 14A and 14B, gray traces). At slower pacing rates, APD was minimally affected by CaMK suppression. However, the peak Ca^{2+} concentration was markedly reduced, especially at faster rates (Figure 14C).

Currents Participating in Steady State APD Rate Dependence and APD Restitution

In order to describe the mechanisms underlying steady state rate dependence and restitution of the APD in the model, it is instructive to first systematically determine which currents participate in these phenomena. In Figure 15, currents were plotted versus V_m during steady state and S1S2 restitution pacing for a variety of CLs and DIs, respectively. If I–V curves are CL or DI independent (i.e. curves overlap), then that current did not participate in steady state rate dependence or restitution, respectively. Conversely, if I–V curves depended greatly on CL or DI, then that current played at least some role in these phenomena.

As CL or DI decreased, fast I_{Na}, responsible for the maximum AP upstroke velocity and maximum V_m, was reduced (see Figure 9, and principles detailed in Luo and Rudy[79]). This is because shortened time at resting potential between beats prevents complete recovery from inactivation. Thus, at fast pacing rates, and short DIs, maximum V_m and upstroke velocity were reduced, explaining some of what follows.

During steady state pacing, I_{Ks} was strongly rate dependent (Figure 15A). The I–V curves were dramatically different at different pacing CLs. However, I_{Ks} was a relatively small contributor to the rate dependence of APD because I_{Ks} density in

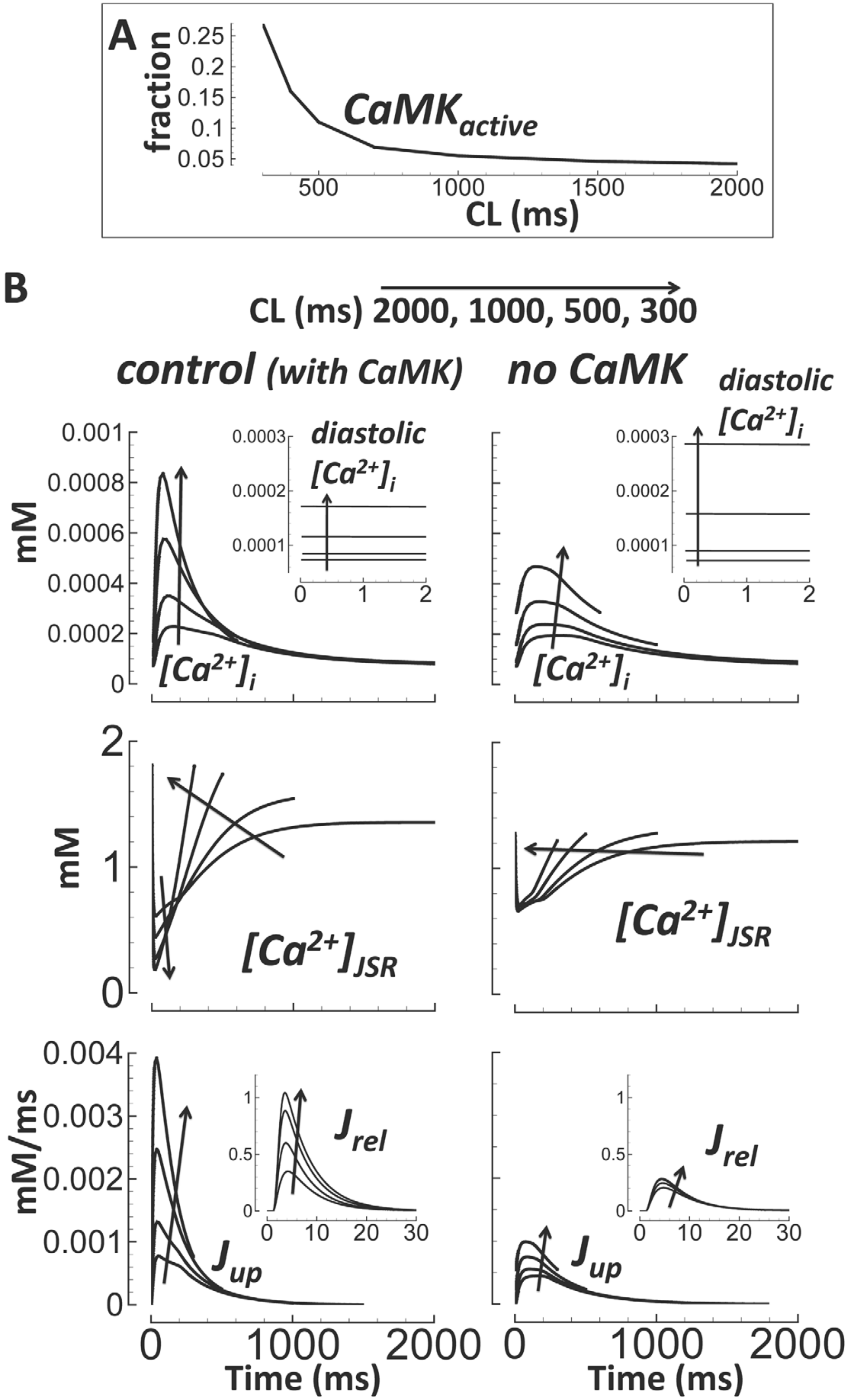

Figure 13. CaMK and Ca^{2+} cycling. A) Rate dependence of CaMK active fraction. B) Ca^{2+} cycling under control conditions (left) and without CaMK (right). CL changes are indicated by arrows. Top) [Ca^{2+}]$_i$ and diastolic values (inset). Middle) [Ca^{2+}]$_{JSR}$. Bottom) J$_{up}$ and J$_{rel}$ (inset, expanded time scale).
doi:10.1371/journal.pcbi.1002061.g013

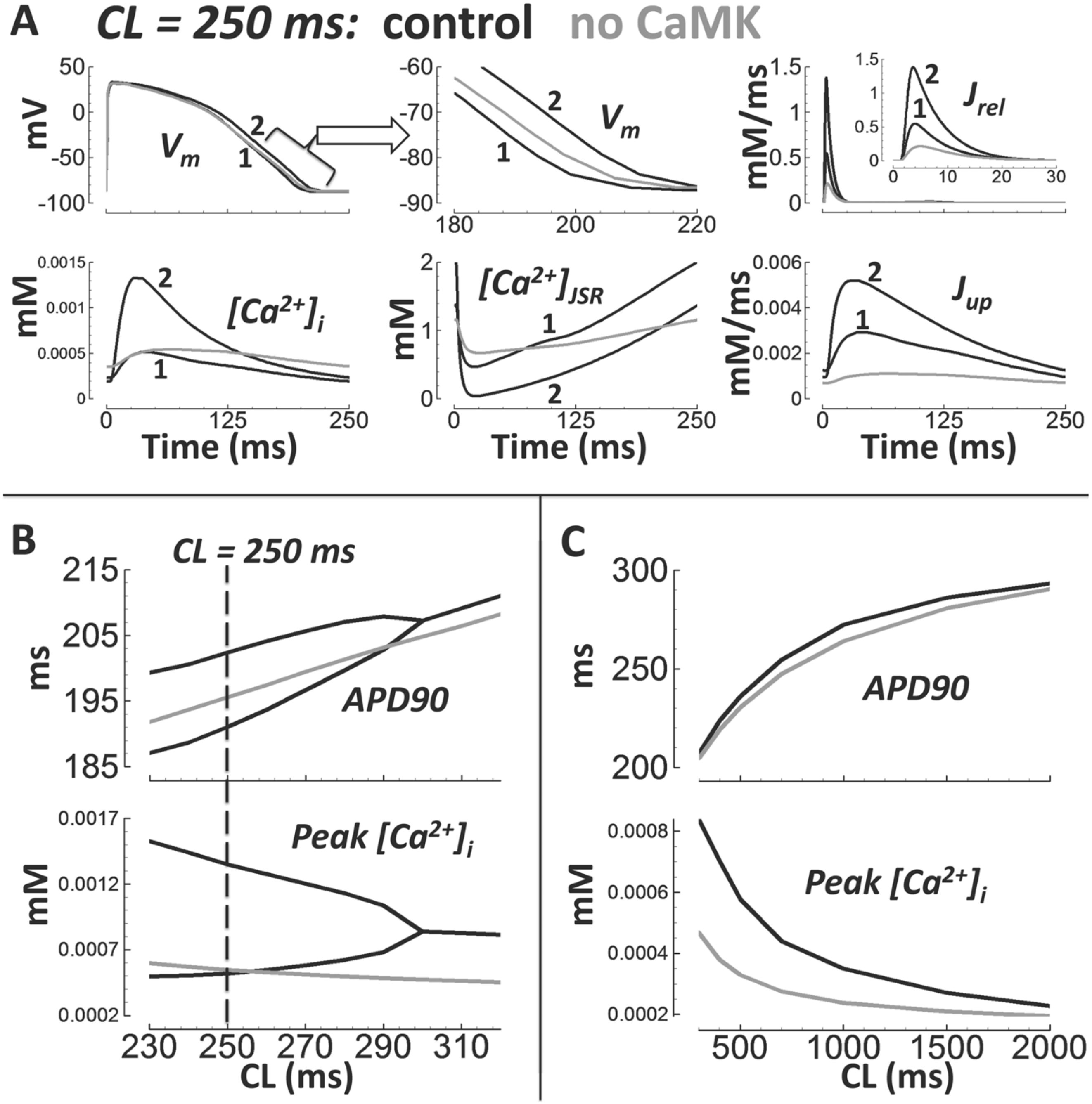

Figure 14. AP and Ca^{2+} alternans at fast pacing. Black lines are control. Gray lines are without CaMK. The two consecutive beats are labeled 1 and 2. A) Pacing at CL = 250 ms. From left to right, top to bottom: AP, expanded time scale showing AP repolarization, J_{rel} (inset is expanded time scale), $[Ca^{2+}]_i$, $[Ca^{2+}]_{JSR}$, and J_{up}. B) Rate dependence of APD (top) and peak $[Ca^{2+}]_i$ (bottom) at fast rates (alternans bifurcations disappear without CaMK). C) Same as panel B, but at slower rates (no bifurcations).
doi:10.1371/journal.pcbi.1002061.g014

human ventricle is small under basal conditions (no β-adrenergic stimulation), and changes relative to slow rate values produced minimal additional outward current at fast rates.

Late I_{Na}, I_{CaL}, I_{NaCa} and I_{NaK} also showed CL dependent changes during steady state pacing (Figure 15A). I_{NaK} became more outward at fast rates. The changes in I_{NaK} were dramatic, and the current density was relatively large. Thus, I_{NaK} was an important contributor to APD shortening at fast pacing rates. Late I_{Na} became dramatically less inward at fast rates, making it a secondary contributor to APD shortening at fast rates. Changes in I_{CaL} and I_{NaCa} opposed APD shortening at fast rates; these currents became more inward at short CLs. I_{NaCa} increased to match the increased Ca^{2+} extrusion burden. Importantly, I_{CaL} increased despite reduced channel availability. I_{CaL} inactivation gates recovered less between beats as pacing rate increased (~20% less at CL = 300 ms compared to CL = 2000 ms). The same mechanism caused reduced late I_{Na} at fast rates (availability at CL = 300 ms was ~1/3 that at CL = 2000 ms). However,

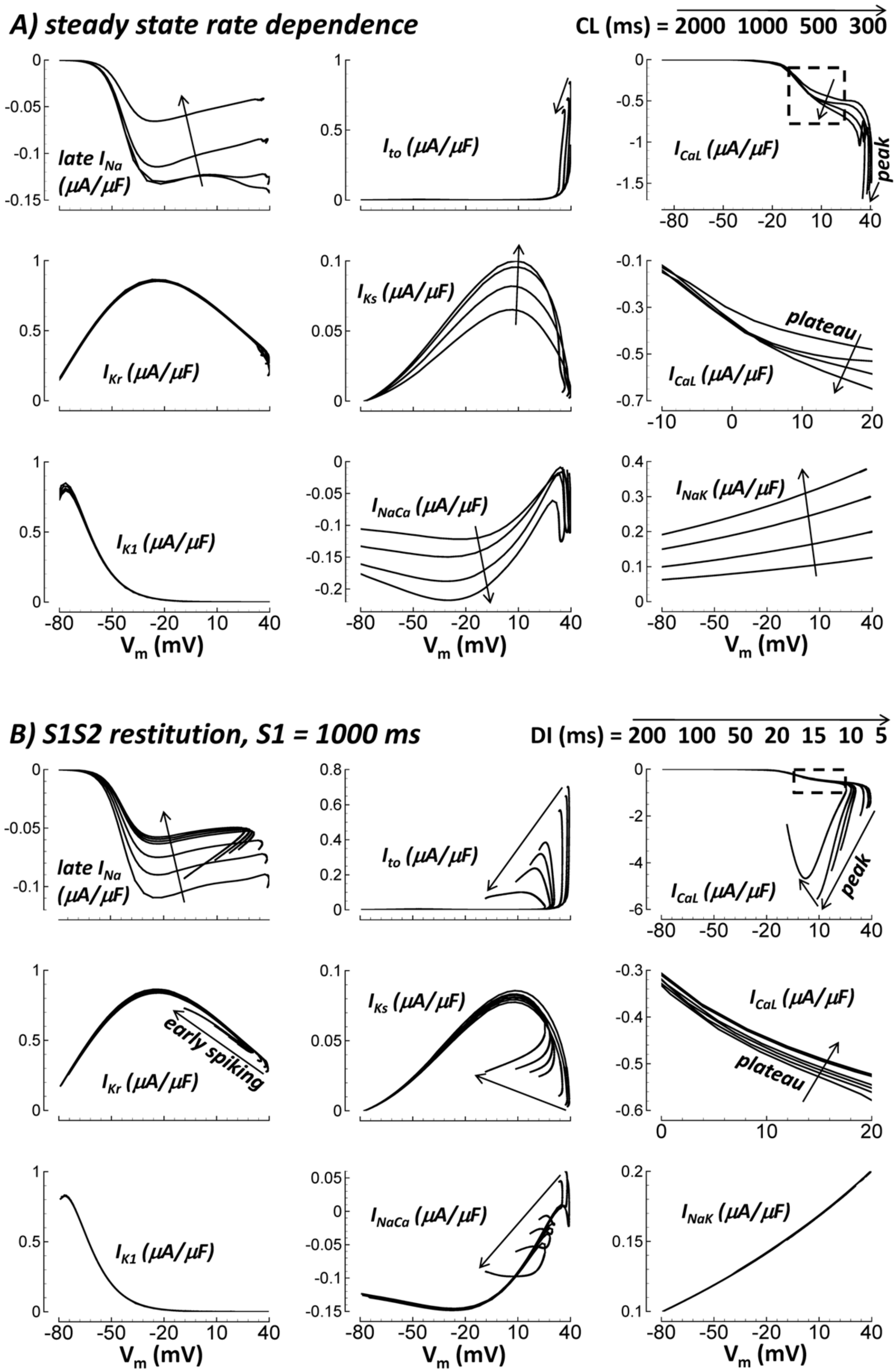
A) steady state rate dependence
CL (ms) = 2000 1000 500 300
late I_{Na} (μA/μF)
I_{to} (μA/μF)
I_{CaL} (μA/μF)
peak
I_{Kr} (μA/μF)
I_{Ks} (μA/μF)
plateau
I_{K1} (μA/μF)
I_{NaCa} (μA/μF)
I_{NaK} (μA/μF)
V_m (mV)
B) S1S2 restitution, S1 = 1000 ms
DI (ms) = 200 100 50 20 15 10 5
late I_{Na} (μA/μF)
I_{to} (μA/μF)
I_{CaL} (μA/μF)
peak
I_{Kr} (μA/μF)
early spiking
I_{Ks} (μA/μF)
plateau
I_{K1} (μA/μF)
I_{NaCa} (μA/μF)
I_{NaK} (μA/μF)
V_m (mV)
-80 -50 -20 10 40

Figure 15. I–V curves during steady state rate dependent pacing at various CLs (panel A), and S1S2 restitution at various DIs (panel B). Arrows indicate decreasing CL or DI. From left to right, top to bottom, results for late I_{Na}, I_{to}, I_{CaL}, I_{Kr}, I_{Ks}, zoom of plateau I_{CaL} (dashed box section), I_{K1}, I_{NaCa}, and I_{NaK} are shown.
doi:10.1371/journal.pcbi.1002061.g015

influences of increased CaMK facilitation combined with increased driving force (reduced maximum V_m) actually caused I_{CaL} to become larger at fast rates.

If Na^+ is clamped to small values associated with slow pacing ($[Na^+]_i$ and $[Na^+]_{ss} = 6.2$ mM at CL = 2000 ms), preventing its accumulation at fast rates, I_{NaK} remains small and CL independent (this mechanism is described later in detail), causing plateau voltages to become relatively CL independent. Thus, with Na^+ clamp, I_{CaL} changes with pacing rate are different than under control conditions. CL independent plateau voltages confer CL independence to the driving force for plateau I_{CaL}. Na^+ clamping reduced Ca^{2+} (via I_{NaCa}) which reduced activated CaMK and thus I_{CaL} facilitation. An interesting consequence is that with Na^+ clamp, I_{CaL} changes with CL help to cause APD shortening at fast rates, whereas in control (i.e. no Na^+ clamp), I_{CaL} changes with CL oppose APD shortening.

During restitution, late I_{Na}, I_{to}, I_{CaL}, I_{Ks} and I_{NaCa} showed DI dependent changes (Figure 15B). Dramatically less inward late I_{Na}

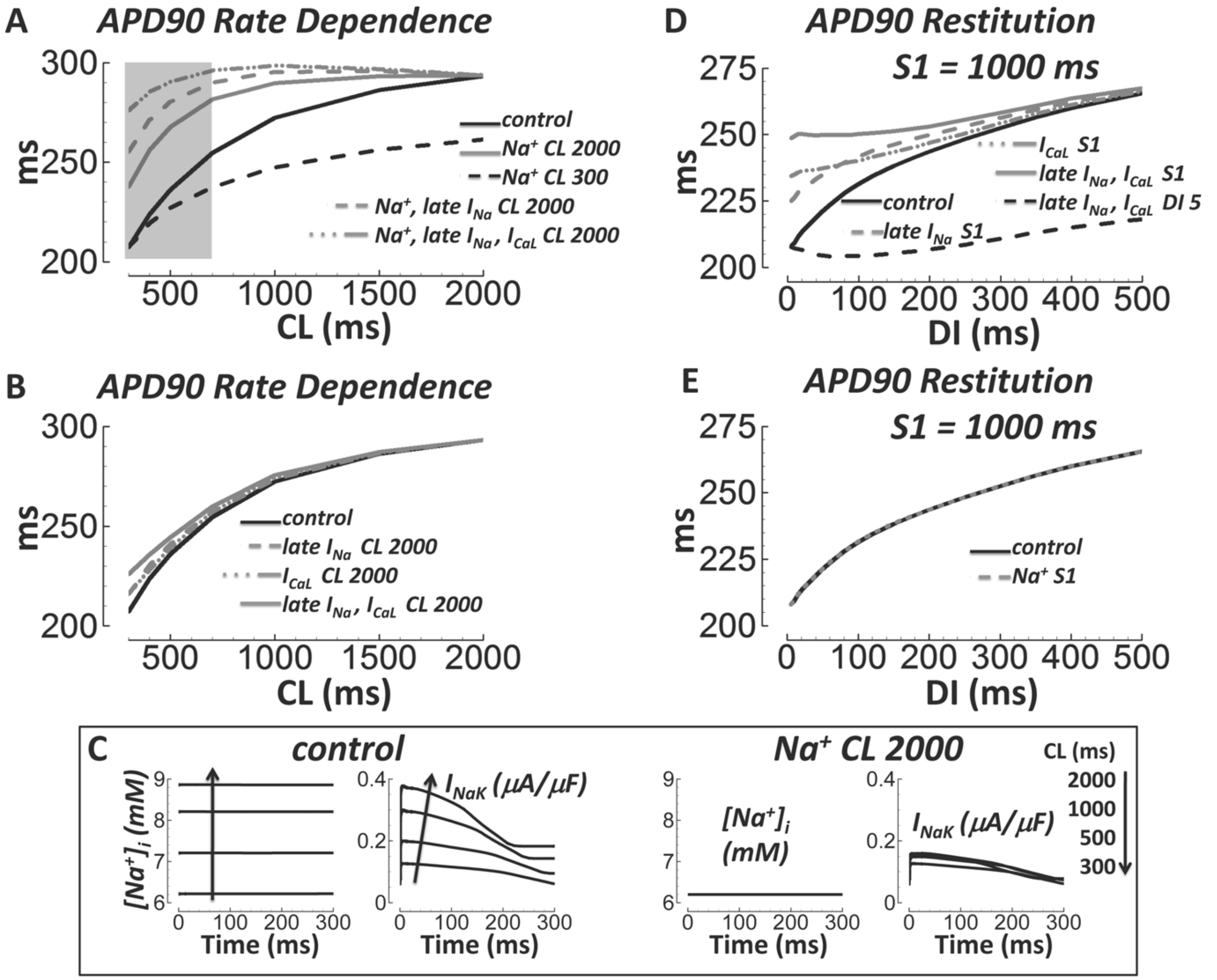

Figure 16. Major causes of steady state APD rate dependence and S1S2 APD restitution. A) APD rate dependence in control (solid black), and with $[Na^+]_i$ and $[Na^+]_{ss}$ clamped to slow rate (solid gray) or fast rate (dashed black) values. When late I_{Na} (dashed gray) or both late I_{Na} and I_{CaL} inactivation gates were reset to their slow rate values (dash-dot-dot gray) in addition to $[Na^+]_i$ and $[Na^+]_{ss}$ slow rate clamp, APD lost almost all rate dependence. Note that slow rate $[Na^+]_i$ and $[Na^+]_{ss}$ clamp alone left residual APD rate dependence, especially at fast rates (CL = 300 to 700 ms, shaded box). B) APD rate dependence (control, solid black) was largely unaffected by resetting inactivation gates for late I_{Na} (dashed gray), I_{CaL} (dash-dot-dot gray), or late I_{Na} and I_{CaL} (solid gray) to their slow rate values (no $[Na^+]_i$ and $[Na^+]_{ss}$ clamping to slow rate values). C) $[Na^+]_i$ and I_{NaK} increase with pacing rate under control conditions (left). When $[Na^+]_i$ and $[Na^+]_{ss}$ are clamped to slow rate values, I_{NaK} is small and rate independent (right). D) APD restitution in control (solid black), and when inactivation gates were reset to S1 values upon S2 delivery (late I_{Na} reset – dashed gray, I_{CaL} reset – dash-dot-dot gray, late I_{Na} and I_{CaL} reset – solid gray). Shown in dashed black is resetting late I_{Na} and I_{CaL} inactivation to the DI = 5 ms value. E) $[Na^+]_i$ and $[Na^+]_{ss}$ clamp to S1 values (dashed gray) did not affect APD restitution (control, solid black).
doi:10.1371/journal.pcbi.1002061.g016

at short DIs helped shorten the APD. The mechanism was reduced availability due to residual inactivation at the start of the S2 beat. I_{CaL} was reduced for the same reason. This was evident during the plateau. CaMK facilitation did not depend on DI because Ca^{2+} accumulation (necessary for CaMK activation) is slow, occurring only after long term pacing to steady state. Similarly, Na^+ did not accumulate at short DIs, which kept I_{NaK} constant. Therefore, plateau potentials and I_{CaL} driving force during the plateau were relatively DI independent. Just as in the case of Na^+ clamp, these properties combined to allow reduced availability of I_{CaL} at short DI to dominate the behavior. However, reduced maximum V_m increased the driving force during the time of peak I_{CaL}, which caused peak current to generally increase at short DIs. At extreme DI of 5 ms, the slow AP upstroke (i.e. reduced dV_m/dt) caused mild I_{CaL} inactivation coincident with activation, so the peak current was reduced compared to DI = 10 ms.

Changes in other currents (I_{to}, I_{Ks} and I_{NaCa}), though nonzero, were relatively minor due to timing. DI dependent changes that increased or reduced current during phase-1 of the AP had little effect on final repolarization time. The exception is I_{Kr}. I_{Kr} is large enough that early spiking helped shorten APD at very short DIs (detailed simulations follow).

Ionic Basis for APD Rate Dependence and Restitution

Steady state rate dependence of the APD was largely caused by accumulation of intracellular Na^+ at fast rates. This is illustrated in Figure 16A. When $[Na^+]_i$ and $[Na^+]_{ss}$ were clamped to values from steady state pacing at CL = 2000 ms, APD lost much of its sensitivity to pacing rate and remained relatively long. Conversely, when the clamp was to $[Na^+]_i$ and $[Na^+]_{ss}$ from steady state pacing at CL = 300 ms, the APD remained relatively short at all rates. Pacing rate dependent $[Na^+]_i$ and $[Na^+]_{ss}$ changes are linked to the AP via I_{NaK}, which responds to $[Na^+]_i$ levels. I_{NaK} increased with $[Na^+]_i$ at fast rate. However it did not increase, regardless of the pacing rate, when $[Na^+]_i$ and $[Na^+]_{ss}$ were kept low (Na^+ at CL = 2000 ms; Figure 16C, right). Moreover, APD remained long at all CLs when I_{NaK} was clamped to its slow rate waveform (not shown).

Steady state APD rate dependence was not completely eliminated by Na^+ clamp alone. That is, clamping $[Na^+]_i$ and $[Na^+]_{ss}$ to slow rate values did not cause APD curves to become absolutely flat with respect to CL, especially at fast pacing rates (Figure 16A, shaded box CL = 300 to 700 ms, solid gray line). This signifies that other mechanisms are involved. When in addition to clamping $[Na^+]_i$ and $[Na^+]_{ss}$ to their slow rate values, we also reset the inactivation gates for late I_{Na}, and especially for both late I_{Na}

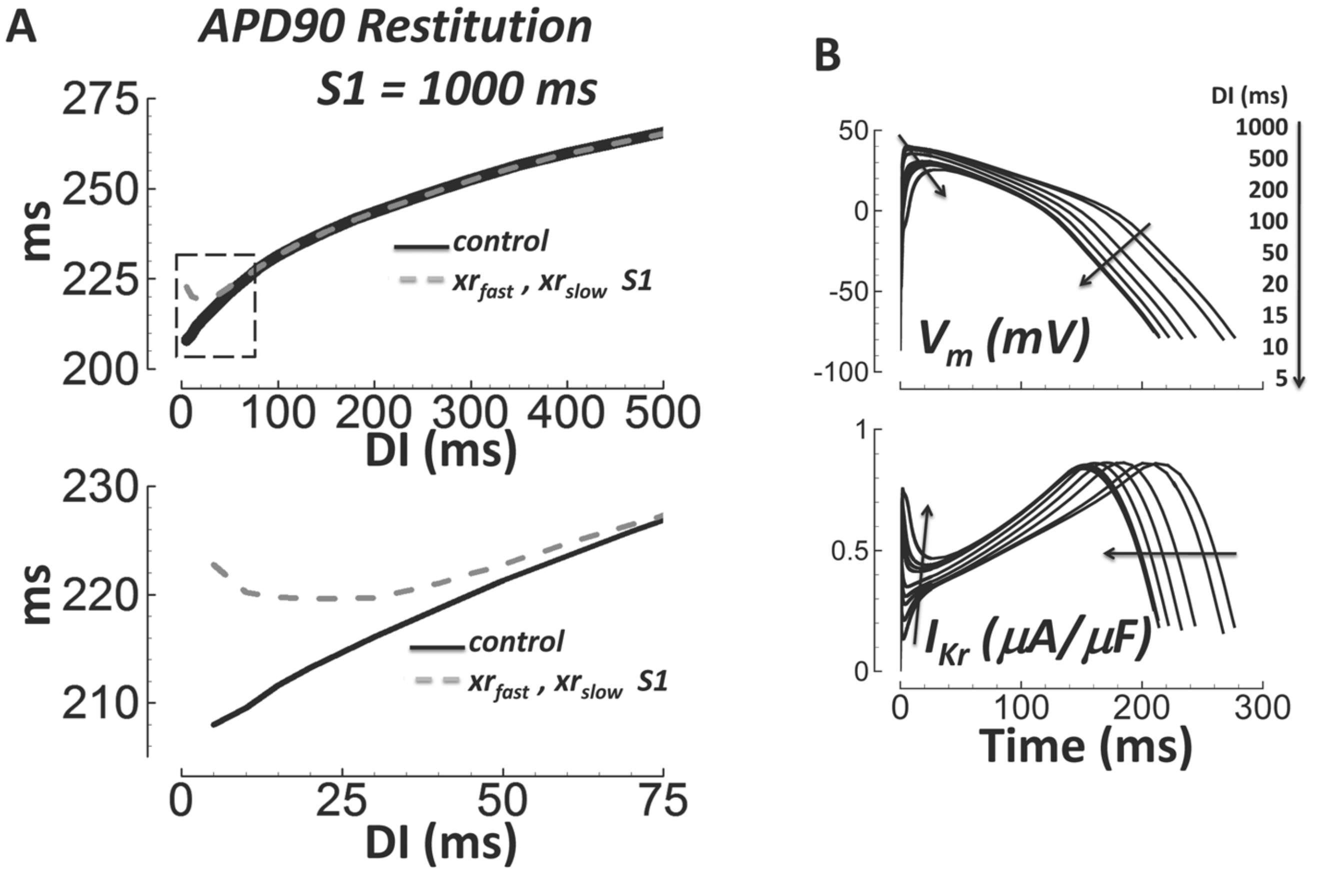

Figure 17. I_{Kr} deactivation is important for APD restitution at very short DIs. A) APD restitution in control (solid black), and when the fast and slow deactivation gates (xr_{fast} and xr_{slow}) were reset to the DI = S1 = 1000 ms value at the start of the S2 beat (dashed gray). Bottom) Zoom in to more clearly show the consequence of deactivation resetting at short DIs (section outlined by dashed box above). B) Traces for the AP (top) and I_{Kr} (bottom) during the S2 beat at different DIs (indicated by arrows). Spiking in I_{Kr} occurred early during the AP at short DI. Spiking was caused by slow deactivation, increasing availability of I_{Kr}.

doi:10.1371/journal.pcbi.1002061.g017

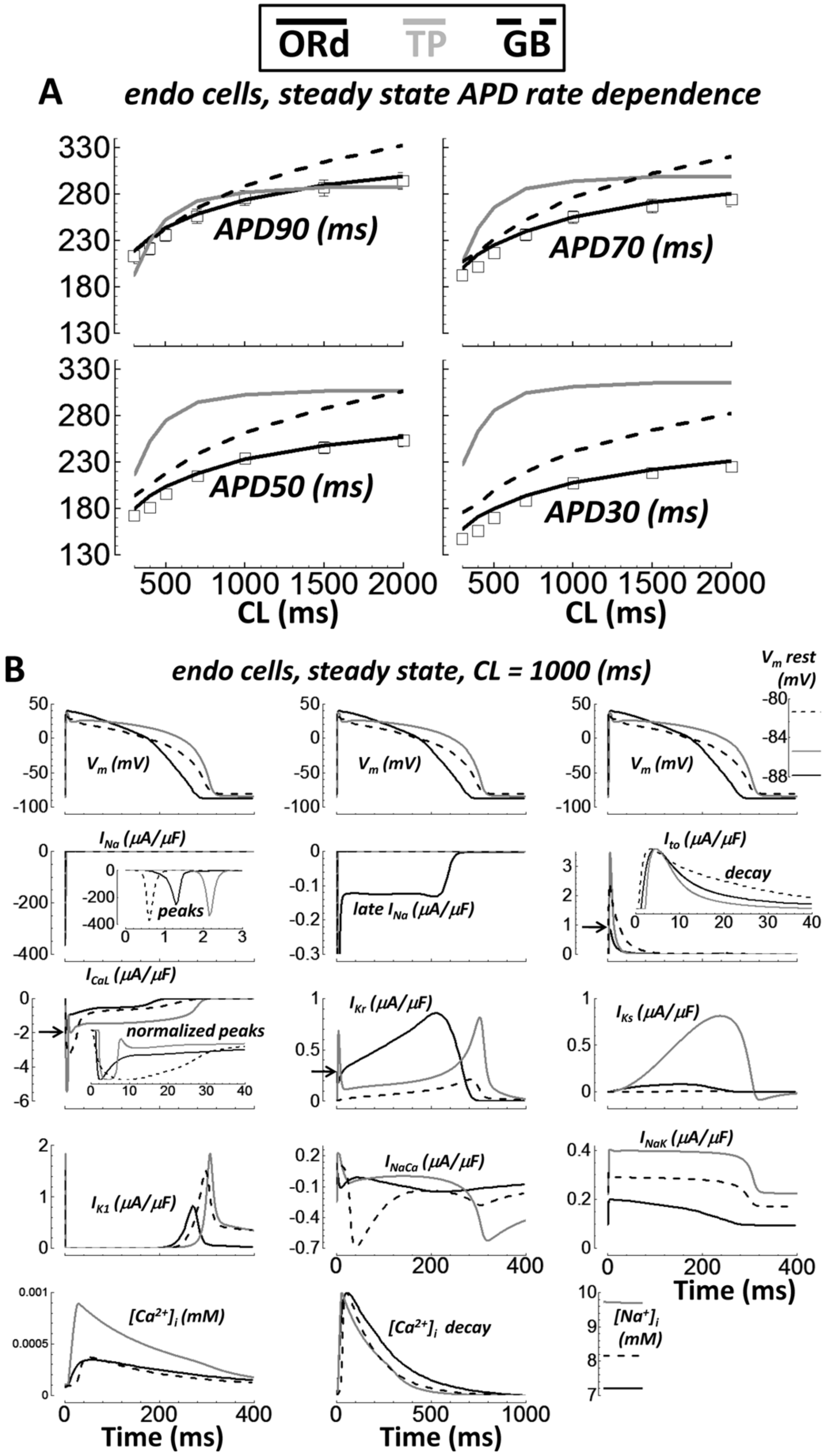
ORd
TP
GB
A
endo cells, steady state APD rate dependence
APD90 (ms)
APD70 (ms)
APD50 (ms)
APD30 (ms)
330
280
230
180
130
500 1000 1500 2000
CL (ms)
B
endo cells, steady state, CL = 1000 (ms)
V_m rest (mV)
-80
-84
-88
V_m (mV)
50
0
-50
-100
I_{Na} (μA/μF)
peaks
late I_{Na} (μA/μF)
I_{to} (μA/μF)
decay
I_{CaL} (μA/μF)
normalized peaks
I_{Kr} (μA/μF)
I_{Ks} (μA/μF)
I_{K1} (μA/μF)
I_{NaCa} (μA/μF)
I_{NaK} (μA/μF)
$[Ca^{2+}]_i$ (mM)
$[Ca^{2+}]_i$ decay
$[Na^+]_i$ (mM)
10
9
8
7
0 200 400
0 500 1000
Time (ms)

Figure 18. Comparison with other human ventricular AP models. Single endo cell simulations from ORd, TP, and GB models are solid black, gray, and dashed black lines, respectively. Experimental results (small tissue preparations) are white squares. A) APD rate dependence. Results for APD90, 70, 50 and 30 are shown top left, top right, bottom left, and bottom right, respectively. B) The AP, major currents, $[Na^+]_i$, and $[Ca^{2+}]_i$ at steady state for CL = 1000 ms. From left to right, top to bottom: AP (with V_m rest inset at far right), I_{Na} (inset shows peaks), late I_{Na} (not present in TP or GB models), I_{to} (inset shows decay rate), I_{CaL} (arrow shows ORd peak magnitude; inset shows normalized peaks, which are wide in TP and GB), I_{Kr} (arrow shows ORd early spike peak magnitude), I_{Ks}, I_{K1}, I_{NaCa}, I_{NaK}, $[Ca^{2+}]_i$, $[Ca^{2+}]_i$ decay rate, and $[Na^+]_i$.
doi:10.1371/journal.pcbi.1002061.g018

and I_{CaL} to their CL = 2000 ms values at the start of each beat, the APD curve flattened further at fast rates (Figure 16A, dashed gray and dashed-dot-dot gray lines, respectively). Importantly, resetting these inactivation gates alone, without also clamping Na^+, had little effect on APD rate dependence (Figure 16B).

As described previously, without Na^+ clamp, fast pacing caused late I_{Na} reduction and I_{CaL} increase; the former helped while the latter opposed APD shortening. However, with Na^+ clamp, both currents became less inward with fast pacing. Thus, resetting I_{CaL} inactivation gates to slow rate values had different effects with, versus without Na^+ clamping. Na^+ clamp prolonged the APD. The prolongation and changed I_{CaL} behavior after Na^+ clamp rendered late I_{Na} and I_{CaL} gate resetting more potent effectors of further AP prolongation; especially at fast rates where residual inactivation between beats was substantial.

Rate dependent Na^+ changes only occurred with the steady state pacing protocol due to slow ion accumulation after lengthy pacing regimes. For APD restitution, clamping $[Na^+]_i$ and $[Na^+]_{ss}$ to values from S1 pacing during the S2 beat did not affect APD (Figure 16E). However, restitution was dramatically affected by resetting inactivation gates for late I_{Na} and/or I_{CaL} to their S1 starting values at the start of the S2 beat (Figure 16D). APD remained long for all DIs. Conversely, when late I_{Na} and/or I_{CaL} inactivation gates were reset to S2 starting values for DI = 5 ms, APD remained short for all DIs. Again, resetting these inactivation gates to their slow rate values had only minor effects on steady state APD rate dependence (Figure 16B).

At very short DIs, I_{Kr} played an important role in APD restitution. In Figure 17A, the fast and slow time dependent deactivation gates (xr_{fast} and xr_{slow}, respectively) were reset to their value at DI = S1 = 1000 ms (dashed gray line, compare to control solid black line). Deactivation of I_{Kr} is slow (Figure 3B). For DI = S1, deactivation was complete between beats. At short DIs, it was incomplete at the start of the S2 beat, enhancing I_{Kr} availability (early I_{Kr} spiking, Figure 17B, bottom) and outward current that contributes to APD shortening. The enhanced availability only mattered at very short DIs, because at these DIs APD was short enough that increased outward current during phase-1 of the AP affected final repolarization time. Changes to currents during later AP phases 2 and 3 (during the plateau and early repolarization, e.g. late I_{Na} and I_{CaL}), generally have greater impact on the APD. Early I_{Kr} spiking reduced maximum V_m, which affected all other currents, including late I_{Na} and I_{CaL}.

Comparison with Other Human Ventricular AP Models

Several important differences exist between the ORd model presented here and other human models (e.g. TP[9] and GB[10] models). Notably, model differences in the rate of repolarization and EAD formation were examined in direct comparison with experiments (Figures 7C, and Figure 11A, respectively). Readers wishing to simulate the human ventricular AP have a choice of models. To help further differentiate the models, additional comparisons are shown in Figure 18.

Undiseased human ventricular measurements of steady state rate dependence of APD90, 70, 50 and 30 were accurately reproduced by the ORd model (Figure 18A, same data as in Figure 7A). Rate dependence of APD90 is fairly accurate in the TP model. However, rate dependence of APD70, 50 and especially APD30 are not accurate. The GB model repolarization rate is more accurate, but divergence from the measurements is large for APD30. At fast pacing rates, GB model APD90 is accurate. Slow pacing APD90 is long compared with experiments (at CL = 2000 ms, APD90 is ~40 ms longer than in experiments). In addition, APD rate dependence does not plateau at CL = 2000 ms.

In Figure 18B, the AP, major currents, and $[Na^+]_i$ and $[Ca^{2+}]_i$ were compared between models. Simulations were in single endo cells paced to steady state at CL = 1000 ms. Of note, the TP and GB models do not include late I_{Na}. The width of the I_{CaL} peak and the morphology were model dependent. It was "cigar shaped" in the TP model. In the GB model, the I_{CaL} peak was broad and poorly defined. The ORd model I_{CaL} peak was sharp, as seen in undiseased human ventricle experiments (AP clamp, Figure 1D). I_{Kr} was relatively small in the GB model, but shared a similar morphology with the ORd model. The TP I_{Kr} morphology is characterized by an early spike and a wider late spike. The I_{Ks} density in the TP model was much larger than in the other models (~10 fold larger). Density and morphology of I_{NaCa} was model dependent. I_{NaCa} was smallest in the ORd model (based on undiseased human measurements, Figure 2B). I_{NaK} was roughly 1.5 and 2 fold greater in GB and TP models, respectively, compared with ORd. The Ca^{2+} transient peak was much larger in the TP model than in the other models, which were similar to each other. The decay rate of $[Ca^{2+}]_i$ was somewhat slower in the ORd model (accurate to undiseased human measurements; Figure 12 panels C and D). Model $[Na^+]_i$ was 7.2, 8.2, and 9.7 mM in ORd, GB, and TP models, respectively.

Discussion

Though the available undiseased human ventricle dataset has been missing essential elements, several human ventricle AP models have been developed and published. The Priebe and Beuckelmann model[35] lacks human specific data for reformulation of major currents, and so was based in large part on its guinea pig predecessor[80]. The TP model[81] and updated version[9] is easy to use, includes many reformulated currents, and simulates physiological restitution and alternans. However, both the TP and GB[10] models lack sufficient I_{CaL} data for validation, and cannot produce EADs. The GB model includes K^+ current reformulations using undiseased human data for validation, but does not produce AP or Ca^{2+} transient alternans. EADs and alternans are both important mechanisms of arrhythmogenesis and should be reproduced in simulation studies of human arrhythmias. The Iyer et al. model[34] is based almost entirely on data from human channels expressed in non myocytes. Though the expressed channels are human, native myocyte ion channels in the ventricle are composed of a variety of protein isoform combinations, auxiliary subunits, cytoskeletal elements, and membrane lipid composition, all of which may influence channel behavior. Anchoring and other regulatory proteins present in native cells also define the local environment for I_{CaL} in particular[82], but are not present in expression systems.

Fink et al. modified the TP model[36] to include updated I_{Kr} and I_{K1} (with $[K^+]_o$ dependence) formulations, based on undiseased human ventricular measurements. The rate of AP repolarization in this modified scheme is more accurate compared with the original TP model. For these advantages, the model sacrifices runtime speed (Markov formulation is used for I_{Kr}). Other core issues of the TP model carry over to this modified version (incorrect I_{CaL}, non-physiologically large I_{Ks}, and no EAD generation under appropriate conditions).

We believe that the new undiseased human data presented here are essential, and substantially increase human specific model accuracy. Due to extensive validation using these new data, our model reproduces all of the following important physiological behaviors: 1) CDI versus VDI inactivation of I_{CaL}; 2) reformulated, detailed and accurate kinetics (using weighted time constants) for I_{to}, I_{NaCa}, I_{K1}, I_{Kr}, I_{Ks}, fast I_{Na}, and late I_{Na}; 3) AP repolarization rate from 30% to 90% repolarization; 4) APD at all physiological pacing rates with/without block of major currents, 5) APD restitution with/without block of delayed rectifier currents; 6) transmural heterogeneity causing upright pseudo-ECG T-wave; 7) early afterdepolarizations (EADs); 8) effects of CaMK; and 9) AP and Ca^{2+} transient alternans.

EADs and Repolarization Rate

One of the most important aspects of the model is its close correspondence to experimental measurements of not only APD90, but also to APD30, 50 and 70 at all physiologically relevant pacing rates and for S1S2 restitution. This large pool of data has previously been unavailable. Accurate repolarization rate (i.e. time between APD30 and 90) for the restitution protocol is crucial for simulating any phenomenon related to reentrant arrhythmia, where head-tail interactions determine refractoriness and vulnerability[83]. Use of new undiseased data for currents that are active during the plateau and phase-3 of the AP (I_{CaL}, I_{NaCa}, I_{Kr} and I_{Ks}) contributed to the correct repolarization rate.

The rate of repolarization and its effects on I_{CaL} control EAD formation in this model, as in canonical EAD explanations [75,84]. Failure of the TP and GB models to reproduce EADs may be due in part to their accelerated repolarization rates (Figure 7C). It may also be caused by inaccurate formulation of I_{CaL} inactivation, developed in absence of the essential undiseased human data presented here.

Steady State APD Rate Dependence

Due to the small amplitude and rapid deactivation kinetics of I_{Ks} in the human ventricle in absence of β-adrenergic stimulation, it does not play a major role in determining APD, APD rate dependence, or APD restitution under basal conditions[85] (Figure 8). This is in contrast to guinea pig ventricle, where slower deactivation and larger amplitude I_{Ks} make it the most important current for steady state APD rate dependence (simulations[86] and experiments[87]). Phosphorylation by PKA in the case of β-adrenergic stimulation greatly enhances both the activation rate and amplitude of I_{Ks}[88]. With β-adrenergic stimulation, I_{Ks} plays an important role in steady state APD rate dependence[89]. Clearly, I_{Ks} is important under various circumstances – the AP repolarizes in human ventricle experiments even when I_{Kr} is blocked[85], and clinical long QT syndrome type 1 is caused by I_{Ks} loss of function[90]. Typically, isolated myocyte patch clamp experiments underestimate I_{Ks} due to enzymatic degradation[42]. In ORd, the role of I_{Ks} was validated using small tissue preparations, where selective I_{Ks} block prolonged APD, but only very modestly under basal conditions (no β-adrenergic stimulation, <15 milliseconds in experiments and simulations at $CL = 1000$ ms, Figure 8).

Block of I_{Kr} caused the most severe changes to the human AP (rate dependence and restitution, Figure 8). However, Supplement Figure S5 in Text S1, and Figure 15A show that I_{Kr} is rate independent, as in experiments[39] and therefore was not responsible for causing APD changes with pacing rate. Rather, our simulations identified rate dependent changes in I_{NaK} secondary to $[Na^+]_i$ accumulation as a primary cause of APD rate dependence (Figure 16A, 16C). This finding is not new. Simulations in dog ventricle[19], human atrium[91], and in the GB human ventricle[10] models all led to this conclusion. However, findings from the Iyer human model[34] differ, at least in part, regarding this mechanism. In the Iyer model, $[Na^+]_i$ affected APD rate dependence via I_{NaCa}, which is primarily outward at fast rates. Rate dependence in the TP model[9] is less $[Na^+]_i$ dependent because, as Grandi discussed[10], I_{Ks} is exaggerated. Experiments by Pieske et al.[57] investigated $[Na^+]_i$ in heart failure, versus nonfailing human ventricular myocytes. Pieske experiments demonstrate that rate dependent $[Na^+]_i$ accumulation is an important phenomenon in health and disease. However, additional experiments are needed to determine whether and how $[Na^+]_i$ affects I_{NaK} and APD in human ventricle.

In addition to I_{NaK} and I_{NaCa} (both included in the ORd model), intracellular Na^+ is also mediated by fluxes related to H^+, CO_2, and HCO_3^- homeostasis. Exchangers and cotransporters move Na^+ ions down the electrochemical gradient in order to offset the cost of H^+, CO_2, and HCO_3^- pumping. Na^+ rate dependent handling and consequently I_{NaK} should be affected by these processes, which were not explicitly included in the ORd model. In the absence of H^+, CO_2, and HCO_3^- fluxes, it is possible that the role of I_{NaK} might have been over estimated. It is important to address this because I_{NaK} and its response to Na^+ accumulation was a major cause of APD rate dependence in the model. Thus, we performed simulations where H^+, CO_2, and HCO_3^- effects on Na^+ were explicitly included, using Crampin and Smith equations[92] (Supplement Figure S12 in Text S1).

Quantitative details of Na^+ handling, I_{NaK} and APD rate dependence were affected when we included H^+, CO_2, and HCO_3^- handling processes. However, the qualitative outcomes were not affected. I_{NaK} increase with fast pacing, secondary to Na^+ accumulation, was still the primary determinant of APD rate dependence during steady state pacing.

Removal of the effects of Na^+ accumulation on steady state APD rate dependence by clamping $[Na^+]_i$ and $[Na^+]_{ss}$ did not completely eliminate APD rate dependence. Especially at fast rates (Figure 16A, shaded box $CL = 300$ to 700 ms, solid gray line), APD was not absolutely flat with respect to CL. APD rate dependence was largely unaffected by resetting inactivation gates for late I_{Na}, and/or I_{CaL} to their slow rate values at the start of each beat (Figure 16B). Interestingly, if these gates were reset while also clamping Na^+ to slow rate values, the APD-CL curve became almost completely flat, even at fast rates (Figure 16A, dashed gray and dashed-dot-dot gray lines, respectively). Thus, accumulation of Na^+ and consequent effects on I_{NaK} is a major cause of APD rate dependence, however, not the only cause. Other currents also participate at fast pacing rates. Though the GB model[10] demonstrated the Na^+/I_{NaK}/APD rate dependence mechanism, it did not show the additional effects of late I_{Na} and I_{CaL}. The GB model cannot show these multi-factorial causes of APD rate dependence because it does not include late Na^+ current (Figure 18), and because I_{CaL} kinetics are inaccurate due to lack of experimental data.

Due to charge conservation, accumulation of $[Na^+]_i$ is associated with an equal reduction in $[K^+]_i$ and a volume converted $[K^+]_o$ increase in tissue clefts and interstitial spaces[93]. This can affect behavior by increasing I_{K1} (its $[K^+]_o$ sensitivity is included in this model), which depolarizes resting voltage and reduces excitability. However, our simulations represent experiments in an isolated myocyte in a large bath, where $[K^+]_o$ is constant. Even *in vivo*, $[K^+]_o$ is tightly controlled via regulation by the lymphatic system and kidneys.

APD Restitution

We showed that in contrast to steady state rate dependence, $[Na^+]_i$ had no effect on APD restitution. Rather, restitution was primarily caused by the time course of recovery from inactivation of late I_{Na} and I_{CaL}; processes which had little effect on steady state-rate dependence of APD (absent Na^+ clamp). At very short DIs, slow deactivation of I_{Kr} caused increased availability and spiking, which helped shorten the APD. APD rate dependence was caused primarily by concentration changes, while APD restitution was caused by gating kinetics. Previous studies have not made this important distinction between steady state rate dependence and restitution mechanisms in human. The role of I_{CaL} and its inactivation kinetics in APD restitution reiterates the primacy of I_{CaL} in determining basic physiological behaviors, highlighting the importance of the new I_{CaL} experimental data, presented here, to model development and validation.

A role for late I_{Na} in restitution could not have been hypothesized using TP or GB models, which have no late I_{Na}. The density of late I_{Na} was constrained in the ORd model by experiments from nonfailing human ventricular myocyte measurements by Maltsev et al.[51], where the late current was measured 200 ms after the start of the voltage clamp step (~0.35 $\mu A/\mu F$ I–V curve maximum). The maximum late I_{Na} during the free running AP model was much smaller (~0.15 $\mu A/\mu F$, about half the I–V curve maximum) even at slow pacing rates, where late I_{Na} was largest. Late current is difficult to measure directly, and it is possible that the current density was overestimated due to selection bias. That is, late I_{Na} is small, and not all cells produced measureable late current (2 of 3 myocytes[51]). However, we consider the model density of late I_{Na} to be accurate based on model reproduction of experiments which consistently showed substantial APD90 shortening following application of 10 μM mexiletine in undiseased human myocardium (90% late I_{Na} block in simulations, Figure 8A).

Ca^{2+} Cycling, CaMK and Alternans

Previously published human ventricle AP models have not incorporated the CaMK signaling pathway. Our human simulations show, as in dog simulations[31,77], that CaMK plays an important role in determining frequency dependence of Ca^{2+} cycling (Figure 13). The model also shows that the integrated electrophysiological consequence of CaMK effects on target channels is minimal. That is, CaMK suppression had only minor effects on APD rate dependence and AP morphology. At very fast pacing (CLs <300 ms), the Ca^{2+} cycling consequences of CaMK phosphorylation were central to alternans formation. Suppression of CaMK eliminated alternans. CaMK related findings are in agreement with simulations using other models developed by our group[77], models from other groups[94], and experiments[95]. However, experiments showing the effects of pharmacological suppression of CaMK on rate dependent behaviors (e.g. by Wehrens et al.[96] with KN-93 in rabbit) should be performed in human ventricular myocytes to validate model predictions.

Transmural Heterogeneity

The method used for implementation of the transmural cell types (M and epi cell), based on the thoroughly validated endo cell framework, was simplistic. That is, we considered that channel conductance was proportional to transmural gradients in mRNA or protein expression for alpha subunits of ion channels. Only in the case of I_{to} were functional current measurement data available[70]. Staying within error bars for mRNA or protein data[67,68,69], channel conductances were modulated so that the simulated transmural AP differences were consistent with experiments[50,71].

The effect of transmural heterogeneity of accessory β-subunits was not considered in the transmural cell type definitions. However, in the case of I_{Ks}, the KCNE1 β-subunit is transmurally heterogeneous. KCNE1 protein was about two times greater in M-cells compared to epi cells[69]. The presence of KCNE1 carries two important functional consequences 1) ~5 fold slower activation and 2) ~5 fold larger conductance[97]. Therefore, theoretically, twice as much KCNE1 in M-cells may increase the variable stoichiometry ratio of KCNE1 to alpha subunit KCNQ1[98], slowing activation and increasing conductance. We conducted simulations to evaluate the influence of KCNE1 heterogeneity on I_{Ks} and the AP (Supplement Figure S13 and related description in Text S1). Due to the small amplitude of human I_{Ks} in the absence of β-adrenergic stimulation, implementation of KCNE1 heterogeneity did not appreciably affect the AP (Supplement Figures S13 and S19 in Text S1, where transmural APDs are shown to be relatively insensitive to changes in I_{Ks} conductance). Interestingly, the simulated effects of KCNE1 on activation rate and conductance offset one another. That is, slowed activation and larger conductance in M-cells yielded I_{Ks} current that was remarkably close to the control case. Similar results were found for epi cell simulations: the effects of faster activation and reduced conductance were offsetting such that their combined effect was minimal.

APD Accommodation

Steady state rate dependence of APD and APD restitution were the focus of the simulations and experiments in this study. However, the time course of APD response to abrupt changes in pacing rate has been shown in human by Franz et al.[99], and simulated in the TP model by Pueyo et al.[100] as a marker for arrhythmia risk. Simulations of APD accommodation in our model compare favorably to Franz experiments (same pacing protocols used in experiments were used in the simulations, Supplement Figure S14 in Text S1). Single exponential curves were fit to the time dependence of APD changes. For abrupt CL reduction from 750 to 480 ms, the time constant was 250 and 284 seconds in experiments and simulations, respectively. Time constants were 300 and 299 seconds in experiments and simulations, respectively, when CL was abruptly returned to 750 ms. When the CL reduction was more severe, from CL = 750 to 410 ms, the time constants were 252 and 165 seconds, in experiments and simulations, respectively. For return to CL = 750 ms, the time constants were 350 and 289 seconds, respectively. Pueyo used time to 90% accommodation to compare model with experiments demonstrating similar accuracy. Both simulation studies also show initial overshoot, or "notching", as observed and described by Franz.

Parameter Sensitivity

As in Romero et al.[101], we performed a sensitivity analysis to determine factors participating in important model outputs, including 1) steady state APD90 rate dependence (Supplement

Figure S15 in Text S1), 2) S1S2 APD90 restitution (Supplement Figure S16 in Text S1), 3) rate dependence of maximum (systolic) $[Ca^{2+}]_i$ (Supplement Figure S17 in Text S1), 4) rate dependence of $[Na^+]_i$ (Supplement Figure S18 in Text S1), and 5) transmural cell type APD90 at steady state (Supplement Figure S19 in Text S1).

The findings from our analysis were similar to those shown by Romero et al. using the TP human AP model[101]. That is, in ORd and TP models, I_{Kr} and I_{CaL} affect APD90 while I_{CaL}, I_{NaCa}, and I_{NaK} affect peak $[Ca^{2+}]_i$. One important difference is the role for I_{Ks}. A much larger role was played by I_{Ks} in the TP model ($\sim$10 fold larger density than in other human models, Figure 18B). In the TP model, I_{Ks} is responsible for steady state rate dependence of the APD (shown by Grandi et al.[10]).

I_{Kr} conductance changes affect APD90 substantially in our model. This was expected, since I_{Kr} is the largest outward current (also in experiments, Figure 8, and in Romero's analysis using the TP model). Though I_{Kr} affects APD, it is not responsible for its rate dependence. Conductance changes in I_{NaK} did not substantially affect APD90 because I_{NaK} is a relatively small current. Yet, rate dependent changes in I_{NaK} (secondary to Na^+ accumulation at fast rate) were the primary determinant of APD rate dependence. $[Na^+]_i$ at different pacing rates, and thus its relative changes with rate, was by far most sensitive to I_{NaK} conductance (Supplement Figure S18 in Text S1). This supports our strategy for setting I_{NaK} conductance to reproduce rate dependence of $[Na^+]_i$ in nonfailing human myocytes[57].

Computational Tractability and Model Stability

To keep the ORd model computationally efficient and parameters well constrained, the Hodgkin-Huxley formalism was used in formulating current equations. This choice was made as a design principal with the thought that interested users can modularly replace any current or flux with more detailed Markov formulations of mutation or drug effects as desired (e.g.[53,66]). Similarly, intracellular Ca^{2+} handling can be modified (e.g. more spatial detail, Markov ryanodine receptor implementation), or various signaling pathways and related effects on ion channels can be added (e.g.[31,89,102]). The basic ORd model has 41 state variables. In the absence of CaMK and its effects on target currents and fluxes, the number of state variables is 31.

Exclusion of Markov models increases parameter constraint. It also prevents the system of differential-algebraic equations from being overly stiff. This promotes model stability and computational tractability. Using the rapid integration technique described in Supplement Text S1 (Computational Methodology section), the model arrives at true and accurate steady state in under one minute of runtime ($\sim$1000 beats are needed, depending on the CL, Visual C++ running on a desktop PC; more details in Supplement Text S1). ORd equations are all smoothly varying functions, free of singularities and "if" conditionals. Thus, the model can readily be implemented in any of a variety of automated numerical integrators, such as Matlab (The MathWorks Inc.), CellML (http://www.cellml.org/), CHASTE[103], or CARP (CardioSolv LLC.).

Limitations

Direct measurement of I_{NaK} in the undiseased or nonfailing human ventricular myocyte is lacking. Therefore, I_{NaK} was validated by reproduction of important biophysical properties (Supplement Figure S7 in Text S1), and by reproduction of $[Na^+]_i$ rate dependence measured in nonfailing human ventricular myocytes (Pieske et al.[57], Figure 12A). However, independent and direct experimental measurement of I_{NaK} in undiseased or nonfailing human ventricular myocytes would provide additional support for the mechanistic conclusion that I_{NaK} changes secondary to Na^+ accumulation at fast pacing rates is a major determinant of steady state APD rate dependence. This conclusion is consistent with several other modeling studies which proposed the same mechanism (dog ventricle[19], human atrium[91], and human ventricle[10]). The relationship between $[Na^+]_i$, I_{NaK} and steady state APD rate dependence was robust. It was not disrupted by including the effects of Na^+/H^+ and Na^+/HCO_3^- exchange fluxes on Na^+ handling (Crampin and Smith equations[92], Supplement Figure S12 in Text S1). Na^+ accumulation and I_{NaK} response were not the only cause of APD rate dependence in the ORd model. At fast pacing rates (CL = 300 to 700 ms), late I_{Na} and I_{CaL} were also involved (Figure 16A, and related discussion).

Measurements of undiseased human endo APs were performed in small tissue preparations (1–3 gram pieces). This was to avoid possible enzymatic degradation of K^+ channel proteins[40,42], affecting currents and the AP. However, electrical loading in tissue subtly affects behavior[19]. We performed simulations using a multicellular fiber model to include loading effects, which had only minor consequences (Figure S8).

APD was $\sim$275 ms in our human endo preparations at CL = 1000 ms, well matched by the model (273 ms). *In vivo* noninvasive electrocardiographic imaging of the activation-recovery interval, an indicator of the cellular epi APD, was $\sim$260 ms in healthy adults[104]. Human monophasic AP measurements are also in this range[58]. Measurements from Drouin et al. showed longer APDs ($\sim$350 ms in endo cells on the cut transmural face at CL = 1000 ms). Having validated the endo model based on more than 100 of our own endo AP measurements, we thought it reasonable to use Drouin transmural APD ratios, rather than the uniformly longer APDs themselves, for validation of the transmural cell type models.

The presence of M cell APs in the nonfailing human heart was observed by Drouin et al.[50], and more recently by Glukhov et al.[71]. However, there is controversy regarding the M cell definition and its role in human. Our M cell model was based on data where the M cell was defined by its transmural location. The resulting simulated M cell AP corresponded with the "max cell" observed by Glukhov.

Recently, Sarkar and Sobie developed a method for quantitative analysis of parameter constraint and relationships between parameters and target outputs in AP models[105]. We did not apply this analysis during model development. However, the extensive validation of channel kinetics and the emergent response of the AP to a variety of dynamic pacing protocols, used in development and validation of the model, ensures sufficient parameter constraint. The parameter sensitivity tests we performed were instructive, though relatively limited (conductance changes only). Application of Sarkar and Sobie's analysis to our model is beyond the scope of this paper, but should provide worthwhile insights regarding inter-relatedness of processes in the human ventricle, in addition to formally testing parameter constraint.

Materials and Methods

Characteristics of Human Tissue

During the last 15 years, undiseased hearts were donated for research in compliance with the Declaration of Helsinki and were approved by the Scientific and Research Ethical Committee of the Medical Scientific Board of the Hungarian Ministry of Health (ETT-TUKEB), under ethical approval No 4991-0/2010-1018EKU (339/PI/010). Data from 140 hearts were used in this study. Of these, 78 were from male donors (56%). The average donor age was 41 years old with standard deviation of 12 years.

Tissue Preparation

Tissue transport and ventricular endo preparations were performed as previously described[85]. Tissue was carefully pinned and placed in a modified Tyrodes superfusate (in mM: NaCl 115, KCl 4, $CaCl_2$ 1.8, $MgCl_2$ 1, $NaHCO_3$ 20, and glucose 11, pH 7.35, 37°C), and point stimulation was via bipolar platinum electrodes. Drug solutions were made fresh on the day of use. Drugs included in this study were, in μM: E-4031 1, HMR-1556 1, nisoldipine 1, $BaCl_2$ 100, ryanodine 5, mexiletine 10. Simulated application of these drugs was 70% I_{Kr}[59], and 90% I_{Ks}[60], I_{CaL}[61], I_{K1}[62], RyR[63], and late I_{Na}[64] block, respectively.

Myocyte Isolation

Tissue transport and myocyte isolation for the undiseased donor hearts were as previously described[85]. Myocyte isolation commenced immediately upon arrival in the laboratory, using the perfusion disaggregation procedure, previously described[85].

Electrophysiology

Data were obtained using conventional whole cell patch-clamp techniques. Micropipette fabrication and data acquisition were as described previously for undiseased donor heart[85]. Axopatch 200 amplifiers, Digidata 1200 converters, and pClamp software were used (Axon Instruments/Molecular Devices). Experiments were performed at 37°C.

The standard bath solution contained, in mM: NaCl 144, NaH_2PO_4 0.33, KCl 4.0, $CaCl_2$ 1.8, $MgCl_2$ 0.53, Glucose 5.5, and HEPES 5.0 at pH of 7.4, and pipette solutions contained K-aspartate 100, KCl 25, K_2ATP 5, $MgCl_2$ 1, EGTA 10 and HEPES 5. The pH was adjusted to 7.2 by KOH (+15−20 mM K^+).

For L-type Ca^{2+} current measurement, the bath solution contained in mM: tetraethylammonium chloride (TEA-Cl) 157, $MgCl_2$ 0.5, HEPES 10, and 1 mM $CaCl_2$, or $BaCl_2$, or $SrCl_2$ (pH 7.4 with CsOH). The pipette solution contained (in mM) CsCl 125, TEA-Cl 20, MgATP 5, creatine phosphate 3.6, EGTA 10, and HEPES 10 (pH 7.2 with CsOH).

For Na^+/Ca^{2+} exchange current measurement, the bath solution contained, (in mM): NaCl 135, CsCl 10, CaCl2 1, $MgCl_2$ 1, $BaCl_2$ 0.2, NaH_2PO_4 0.33, TEACl 10, HEPES 10, glucose 10 and (in μM) ouabain 20, nisoldipine 1, lidocaine 50, pH 7.4. The pipette solution contained (in mM): CsOH 140, aspartic acid 75, TEACl 20, MgATP 5, HEPES 10, NaCl 20, EGTA 20, CaCl2 10 (pH 7.2 with CsOH).

Ca^{2+} Transient Florescence

Isolated myocytes from the undiseased donor hearts were used to measure the Ca^{2+} transient during point stimulation via bipolar platinum electrodes, indicated by Fura-2-AM, as was described previously[106]. Bath temperature was 37°C.

Pacing Protocols

For both experiments and simulations, we determined APD at 30, 50, 70 and 90% of complete repolarization (APD30–90, in ms). The start of the AP was the time of maximum dV_m/dt. The time of APDX occurred once membrane voltage was X% of the resting value. Resting voltage was measured immediately prior to each paced beat. For APD rate dependence, pacing was to steady state. For APD restitution (S1S2, or static restitution), S1 pacing was at cycle length (CL) = 1000 ms. The S2 beat was delivered at variable diastolic intervals (DIs), measured relative to APD90.

The dynamic restitution protocol was simulated as in experiments by Koller et al.[58]. Pacing was at a variety of rates (30 seconds at CLs from 230 to 1000 ms, no S2 beats). APD95 was plotted against DI (where DI = CL – APD95). Unlike static S1S2 restitution, the dynamic restitution protocol allows for more than one APD to be associated with a given DI. This is significant because bifurcation in the dynamic restitution curve is believed to be arrhythmogenic[107].

Population Based CaMK effects

For all channels affected by CaMK, we created separate models for the fully CaMK phosphorylated channels, and the totally non phosphorylated channels. Then, based on the degree of CaMK activation ($CaMK_{active}$), we determined the proportion of channels affected by CaMK. To calculate the CaMK affected current (or flux), we added the weighted sum of fully affected and totally unaffected channels, using the proportionality. The model employed for CaMK activity was validated previously[31,77].

Relative Weights in a Two Time Constant Scheme

When measurements called for a gating process to be represented by both a fast and a slow process, we included separate fast and slow gates. However, we did not simply multiply fast and slow gates to modulate conductance as others have done previously. To do so allows the fast process alone to completely control deactivation/inactivation, and the slow process alone to completely control activation/recovery. Rather, since measurements of bi-exponential behaviors provide the relative weight of fast/slow processes, we modeled the measurements accordingly, and used the weighted sum of fast and slow processes.

Transmural Wedge Simulation

We computed the pseudo-ECG using a 1-dimensional model of the transmural wedge preparation[108,109]. In brief, the spatially weighted sum of the voltage gradient was determined at a point 2 cm from the epi end of a heterogeneous multicellular fiber, along the fiber axis. Cells 1–60 were endo, 61–105 were M, and 106–165 were epi. The stimulus was delivered to cell 1. Cells 15 from both ends of the fiber were excluded from the gradient measurement due to confounding edge effects. Pacing was for 100 beats using steady state initial conditions from paced single cells.

Equations, Computers, and Software

All model equations, hardware and software used, and rapid integration methods are provided in Supplement Text S1. Model code can be downloaded from the research section of our website: http://rudylab.wustl.edu.

Supporting Information

Text S1 Supplementary materials.
(PDF)

Acknowledgments

Thanks to Norbert Jost from Varró's laboratory, and to members of the Rudy laboratory for helpful discussions and comments on the manuscript. We also thank Jiajing Xu and Jordi Heijman for proofing the Supplement Text S1 equations.

Author Contributions

Analyzed the data: TO LV AV YR. Contributed reagents/materials/analysis tools: TO LV AV YR. Wrote the paper: TO YR. Conceived and designed the simulations and experiments: TO LV AV YR. Performed the simulations and experiments: TO LV.

References

1. Myerburg RJ (2002) Scientific gaps in the prediction and prevention of sudden cardiac death. J Cardiovasc Electrophysiol 13: 709–723.
2. Winslow RL, Cortassa S, O'Rourke B, Hashambhoy YL, Rice JJ, et al. (2010) Integrative modeling of the cardiac ventricular myocyte. Wiley Interdiscip Rev Syst Biol Med DOI: 101002/wsbm122 [Epub ahead of print].
3. Ackerman MJ, Mohler PJ (2010) Defining a new paradigm for human arrhythmia syndromes: phenotypic manifestations of gene mutations in ion channel- and transporter-associated proteins. Circ Res 107: 457–465.
4. Akar FG, Wu RC, Deschenes I, Armoundas AA, Piacentino V, 3rd, et al. (2004) Phenotypic differences in transient outward K+ current of human and canine ventricular myocytes: insights into molecular composition of ventricular Ito. Am J Physiol Heart Circ Physiol 286: H602–609.
5. Blechschmidt S, Haufe V, Benndorf K, Zimmer T (2008) Voltage-gated Na+ channel transcript patterns in the mammalian heart are species-dependent. Prog Biophys Mol Biol 98: 309–318.
6. Zicha S, Moss I, Allen B, Varro A, Papp J, et al. (2003) Molecular basis of species-specific expression of repolarizing K+ currents in the heart. Am J Physiol Heart Circ Physiol 285: H1641–1649.
7. Rudy Y, Ackerman MJ, Bers DM, Clancy CE, Houser SR, et al. (2008) Systems approach to understanding electromechanical activity in the human heart: a national heart, lung, and blood institute workshop summary. Circulation 118: 1202–1211.
8. Rudy Y, Silva JR (2006) Computational biology in the study of cardiac ion channels and cell electrophysiology. Q Rev Biophys 39: 57–116.
9. Ten Tusscher KH, Panfilov AV (2006) Alternans and spiral breakup in a human ventricular tissue model. Am J Physiol Heart Circ Physiol 291: H1088–1100.
10. Grandi E, Pasqualini FS, Bers DM (2010) A novel computational model of the human ventricular action potential and Ca transient. J Mol Cell Cardiol 48: 112–121.
11. Magyar J, Iost N, Kortvely A, Banyasz T, Virag L, et al. (2000) Effects of endothelin-1 on calcium and potassium currents in undiseased human ventricular myocytes. Pflugers Arch 441: 144–149.
12. Fulop L, Banyasz T, Magyar J, Szentandrassy N, Varro A, et al. (2004) Reopening of L-type calcium channels in human ventricular myocytes during applied epicardial action potentials. Acta Physiol Scand 180: 39–47.
13. Aggarwal R, Boyden PA (1995) Diminished Ca2+ and Ba2+ currents in myocytes surviving in the epicardial border zone of the 5-day infarcted canine heart. Circ Res 77: 1180–1191.
14. Findlay I (2002) Voltage- and cation-dependent inactivation of L-type Ca2+ channel currents in guinea-pig ventricular myocytes. J Physiol 541: 731–740.
15. Grandi E, Morotti S, Ginsburg KS, Severi S, Bers DM (2010) Interplay of voltage and Ca-dependent inactivation of L-type Ca current. Prog Biophys Mol Biol 103: 44–50.
16. Ferreira G, Yi J, Rios E, Shirokov R (1997) Ion-dependent inactivation of barium current through L-type calcium channels. J Gen Physiol 109: 449–461.
17. Kim J, Ghosh S, Nunziato DA, Pitt GS (2004) Identification of the components controlling inactivation of voltage-gated Ca2+ channels. Neuron 41: 745–754.
18. Mahajan A, Shiferaw Y, Sato D, Baher A, Olcese R, et al. (2008) A rabbit ventricular action potential model replicating cardiac dynamics at rapid heart rates. Biophys J 94: 392–410.
19. Decker KF, Heijman J, Silva JR, Hund TJ, Rudy Y (2009) Properties and ionic mechanisms of action potential adaptation, restitution, and accommodation in canine epicardium. Am J Physiol Heart Circ Physiol 296: H1017–1026.
20. Peterson BZ, DeMaria CD, Adelman JP, Yue DT (1999) Calmodulin is the Ca2+ sensor for Ca2+ -dependent inactivation of L-type calcium channels. Neuron 22: 549–558.
21. Dzhura I, Wu Y, Colbran RJ, Balser JR, Anderson ME (2000) Calmodulin kinase determines calcium-dependent facilitation of L-type calcium channels. Nat Cell Biol 2: 173–177.
22. Amos GJ, Wettwer E, Metzger F, Li Q, Himmel HM, et al. (1996) Differences between outward currents of human atrial and subepicardial ventricular myocytes. J Physiol 491(Pt1): 31–50.
23. Greenstein JL, Wu R, Po S, Tomaselli GF, Winslow RL (2000) Role of the calcium-independent transient outward current I(to1) in shaping action potential morphology and duration. Circ Res 87: 1026–1033.
24. Tessier S, Karczewski P, Krause EG, Pansard Y, Acar C, et al. (1999) Regulation of the transient outward K(+) current by Ca(2+)/calmodulin-dependent protein kinases II in human atrial myocytes. Circ Res 85: 810–819.
25. Wagner S, Hacker E, Grandi E, Weber SL, Dybkova N, et al. (2009) Ca/calmodulin kinase II differentially modulates potassium currents. Circ Arrhythm Electrophysiol 2: 285–294.
26. Kang TM, Hilgemann DW (2004) Multiple transport modes of the cardiac Na+/Ca2+ exchanger. Nature 427: 544–548.
27. Dong H, Dunn J, Lytton J (2002) Stoichiometry of the Cardiac Na+/Ca2+ exchanger NCX1.1 measured in transfected HEK cells. Biophys J 82: 1943–1952.
28. Fujioka Y, Komeda M, Matsuoka S (2000) Stoichiometry of Na+-Ca2+ exchange in inside-out patches excised from guinea-pig ventricular myocytes. J Physiol 523(Pt2): 339–351.
29. Weber CR, Piacentino V, 3rd, Houser SR, Bers DM (2003) Dynamic regulation of sodium/calcium exchange function in human heart failure. Circulation 108: 2224–2229.
30. Faber GM, Silva J, Livshitz L, Rudy Y (2007) Kinetic properties of the cardiac L-type Ca2+ channel and its role in myocyte electrophysiology: a theoretical investigation. Biophys J 92: 1522–1543.
31. Hund TJ, Rudy Y (2004) Rate dependence and regulation of action potential and calcium transient in a canine cardiac ventricular cell model. Circulation 110: 3168–3174.
32. Frank JS, Mottino G, Reid D, Molday RS, Philipson KD (1992) Distribution of the Na(+)-Ca2+ exchange protein in mammalian cardiac myocytes: an immunofluorescence and immunocolloidal gold-labeling study. J Cell Biol 117: 337–345.
33. Kieval RS, Bloch RJ, Lindenmayer GE, Ambesi A, Lederer WJ (1992) Immunofluorescence localization of the Na-Ca exchanger in heart cells. Am J Physiol 263: C545–550.
34. Iyer V, Mazhari R, Winslow RL (2004) A computational model of the human left-ventricular epicardial myocyte. Biophys J 87: 1507–1525.
35. Priebe L, Beuckelmann DJ (1998) Simulation study of cellular electric properties in heart failure. Circ Res 82: 1206–1223.
36. Fink M, Noble D, Virag L, Varro A, Giles WR (2008) Contributions of HERG K+ current to repolarization of the human ventricular action potential. Prog Biophys Mol Biol 96: 357–376.
37. Bailly P, Mouchoniere M, Benitah JP, Camilleri L, Vassort G, et al. (1998) Extracellular K+ dependence of inward rectification kinetics in human left ventricular cardiomyocytes. Circulation 98: 2753–2759.
38. Konarzewska H, Peeters GA, Sanguinetti MC (1995) Repolarizing K+ currents in nonfailing human hearts. Similarities between right septal subendocardial and left subepicardial ventricular myocytes. Circulation 92: 1179–1187.
39. Jost N, Acsai K, Horvath B, Banyasz T, Baczko I, et al. (2009) Contribution of I Kr and I K1 to ventricular repolarization in canine and human myocytes: is there any influence of action potential duration? Basic Res Cardiol 104: 33–41.
40. Rajamani S, Anderson CL, Valdivia CR, Eckhardt LL, Foell JD, et al. (2006) Specific serine proteases selectively damage KCNH2 (hERG1) potassium channels and I(Kr). Am J Physiol Heart Circ Physiol 290: H1278–1288.
41. Virag L, Iost N, Opincariu M, Szolnoky J, Szecsi J, et al. (2001) The slow component of the delayed rectifier potassium current in undiseased human ventricular myocytes. Cardiovasc Res 49: 790–797.
42. Li GR, Feng J, Yue L, Carrier M, Nattel S (1996) Evidence for two components of delayed rectifier K+ current in human ventricular myocytes. Circ Res 78: 689–696.
43. Tohse N (1990) Calcium-sensitive delayed rectifier potassium current in guinea pig ventricular cells. Am J Physiol 258: H1200–1207.
44. Sakakibara Y, Furukawa T, Singer DH, Jia H, Backer CL, et al. (1993) Sodium current in isolated human ventricular myocytes. Am J Physiol 265: H1301–1309.
45. Nagatomo T, Fan Z, Ye B, Tonkovich GS, January CT, et al. (1998) Temperature dependence of early and late currents in human cardiac wild-type and long Q-T DeltaKPQ Na+ channels. Am J Physiol 275: H2016–2024.
46. Hanck DA, Sheets MF (1992) Time-dependent changes in kinetics of Na+ current in single canine cardiac Purkinje cells. Am J Physiol 262: H1197–1207.
47. Wagner S, Dybkova N, Rasenack EC, Jacobshagen C, Fabritz L, et al. (2006) Ca2+/calmodulin-dependent protein kinase II regulates cardiac Na+ channels. J Clin Invest 116: 3127–3138.
48. Spach MS, Heidlage JF, Dolber PC, Barr RC (2000) Electrophysiological effects of remodeling cardiac gap junctions and cell size: experimental and model studies of normal cardiac growth. Circ Res 86: 302–311.
49. Taggart P, Sutton PM, Opthof T, Coronel R, Trimlett R, et al. (2000) Inhomogeneous transmural conduction during early ischaemia in patients with coronary artery disease. J Mol Cell Cardiol 32: 621–630.
50. Drouin E, Charpentier F, Gauthier C, Laurent K, Le Marec H (1995) Electrophysiologic characteristics of cells spanning the left ventricular wall of human heart: evidence for presence of M cells. J Am Coll Cardiol 26: 185–192.
51. Maltsev VA, Sabbah HN, Higgins RS, Silverman N, Lesch M, et al. (1998) Novel, ultraslow inactivating sodium current in human ventricular cardiomyocytes. Circulation 98: 2545–2552.
52. Maltsev VA, Undrovinas AI (2006) A multi-modal composition of the late Na+ current in human ventricular cardiomyocytes. Cardiovasc Res 69: 116–127.
53. Clancy CE, Rudy Y (1999) Linking a genetic defect to its cellular phenotype in a cardiac arrhythmia. Nature 400: 566–569.

54. Smith NP, Crampin EJ (2004) Development of models of active ion transport for whole-cell modelling: cardiac sodium-potassium pump as a case study. Prog Biophys Mol Biol 85: 387–405.
55. Jansen MA, Shen H, Zhang L, Wolkowicz PE, Balschi JA (2003) Energy requirements for the Na+ gradient in the oxygenated isolated heart: effect of changing the free energy of ATP hydrolysis. Am J Physiol Heart Circ Physiol 285: H2437–2445.
56. Nakao M, Gadsby DC (1989) [Na] and [K] dependence of the Na/K pump current-voltage relationship in guinea pig ventricular myocytes. J Gen Physiol 94: 539–565.
57. Pieske B, Maier LS, Piacentino V, 3rd, Weisser J, Hasenfuss G, et al. (2002) Rate dependence of [Na+]i and contractility in nonfailing and failing human myocardium. Circulation 106: 447–453.
58. Koller ML, Maier SK, Gelzer AR, Bauer WR, Meesmann M, et al. (2005) Altered dynamics of action potential restitution and alternans in humans with structural heart disease. Circulation 112: 1542–1548.
59. Sanguinetti MC, Jurkiewicz NK (1990) Two components of cardiac delayed rectifier K+ current. Differential sensitivity to block by class III antiarrhythmic agents. J Gen Physiol 96: 195–215.
60. Gogelein H, Bruggemann A, Gerlach U, Brendel J, Busch AE (2000) Inhibition of IKs channels by HMR 1556. Naunyn Schmiedebergs Arch Pharmacol 362: 480–488.
61. Walsh KB, Zhang J, Fuseler JW, Hilliard N, Hockerman GH (2007) Adenoviral-mediated expression of dihydropyridine-insensitive L-type calcium channels in cardiac ventricular myocytes and fibroblasts. Eur J Pharmacol 565: 7–16.
62. Warren M, Guha PK, Berenfeld O, Zaitsev A, Anumonwo JM, et al. (2003) Blockade of the inward rectifying potassium current terminates ventricular fibrillation in the guinea pig heart. J Cardiovasc Electrophysiol 14: 621–631.
63. Nanasi PP, Sarkozi S, Szigeti G, Jona I, Szegedi C, et al. (2000) Biphasic effect of bimoclomol on calcium handling in mammalian ventricular myocardium. Br J Pharmacol 129: 1405–1412.
64. Wang DW, Yazawa K, Makita N, George AL, Jr., Bennett PB (1997) Pharmacological targeting of long QT mutant sodium channels. J Clin Invest 99: 1714–1720.
65. Yuan W, Bers DM (1994) Ca-dependent facilitation of cardiac Ca current is due to Ca-calmodulin-dependent protein kinase. Am J Physiol 267: H982–993.
66. Silva J, Rudy Y (2005) Subunit interaction determines IKs participation in cardiac repolarization and repolarization reserve. Circulation 112: 1384–1391.
67. Gaborit N, Le Bouter S, Szuts V, Varro A, Escande D, et al. (2007) Regional and tissue specific transcript signatures of ion channel genes in the non-diseased human heart. J Physiol 582: 675–693.
68. Soltysinska E, Olesen SP, Christ T, Wettwer E, Varro A, et al. (2009) Transmural expression of ion channels and transporters in human nondiseased and end-stage failing hearts. Pflugers Arch 459: 11–23.
69. Szabo G, Szentandrassy N, Biro T, Toth BI, Czifra G, et al. (2005) Asymmetrical distribution of ion channels in canine and human left-ventricular wall: epicardium versus midmyocardium. Pflugers Arch 450: 307–316.
70. Nabauer M, Beuckelmann DJ, Uberfuhr P, Steinbeck G (1996) Regional differences in current density and rate-dependent properties of the transient outward current in subepicardial and subendocardial myocytes of human left ventricle. Circulation 93: 168–177.
71. Glukhov AV, Fedorov VV, Lou Q, Ravikumar VK, Kalish PW, et al. (2010) Transmural dispersion of repolarization in failing and nonfailing human ventricle. Circ Res 106: 981–991.
72. Shimizu W, Antzelevitch C (1998) Cellular basis for the ECG features of the LQT1 form of the long-QT syndrome: effects of beta-adrenergic agonists and antagonists and sodium channel blockers on transmural dispersion of repolarization and torsade de pointes. Circulation 98: 2314–2322.
73. Guo D, Liu Q, Liu T, Elliott G, Gingras M, et al. (2011) Electrophysiological properties of HBI-3000: a new antiarrhythmic agent with multiple-channel blocking properties in human ventricular myocytes. J Cardiovasc Pharmacol 57: 79–85.
74. Thomsen MB, Volders PG, Stengl M, Spatjens RL, Beekman JD, et al. (2003) Electrophysiological safety of sertindole in dogs with normal and remodeled hearts. J Pharmacol Exp Ther 307: 776–784.
75. Zeng J, Rudy Y (1995) Early afterdepolarizations in cardiac myocytes: mechanism and rate dependence. Biophys J 68: 949–964.
76. Schmidt U, Hajjar RJ, Helm PA, Kim CS, Doye AA, et al. (1998) Contribution of abnormal sarcoplasmic reticulum ATPase activity to systolic and diastolic dysfunction in human heart failure. J Mol Cell Cardiol 30: 1929–1937.
77. Livshitz LM, Rudy Y (2007) Regulation of Ca2+ and electrical alternans in cardiac myocytes: role of CAMKII and repolarizing currents. Am J Physiol Heart Circ Physiol 292: H2854–2866.
78. Cutler MJ, Wan X, Laurita KR, Hajjar RJ, Rosenbaum DS (2009) Targeted SERCA2a gene expression identifies molecular mechanism and therapeutic target for arrhythmogenic cardiac alternans. Circ Arrhythm Electrophysiol 2: 686–694.
79. Luo CH, Rudy Y (1991) A model of the ventricular cardiac action potential. Depolarization, repolarization, and their interaction. Circ Res 68: 1501–1526.
80. Luo CH, Rudy Y (1994) A dynamic model of the cardiac ventricular action potential. I. Simulations of ionic currents and concentration changes. Circ Res 74: 1071–1096.
81. ten Tusscher KH, Noble D, Noble PJ, Panfilov AV (2004) A model for human ventricular tissue. Am J Physiol Heart Circ Physiol 286: H1573–1589.
82. Kobayashi T, Yamada Y, Fukao M, Tsutsuura M, Tohse N (2007) Regulation of Cav1.2 current: interaction with intracellular molecules. J Pharmacol Sci 103: 347–353.
83. Hund TJ, Otani NF, Rudy Y (2000) Dynamics of action potential head-tail interaction during reentry in cardiac tissue: ionic mechanisms. Am J Physiol Heart Circ Physiol 279: H1869–1879.
84. Weiss JN, Garfinkel A, Karagueuzian HS, Chen PS, Qu Z (2010) Early afterdepolarizations and cardiac arrhythmias. Heart Rhythm 7: 1891–1899.
85. Jost N, Virag L, Bitay M, Takacs J, Lengyel C, et al. (2005) Restricting excessive cardiac action potential and QT prolongation: a vital role for IKs in human ventricular muscle. Circulation 112: 1392–1399.
86. Faber GM, Rudy Y (2000) Action potential and contractility changes in [Na(+)](i) overloaded cardiac myocytes: a simulation study. Biophys J 78: 2392–2404.
87. Rocchetti M, Besana A, Gurrola GB, Possani LD, Zaza A (2001) Rate dependency of delayed rectifier currents during the guinea-pig ventricular action potential. J Physiol 534: 721–732.
88. Volders PG, Stengl M, van Opstal JM, Gerlach U, Spatjens RL, et al. (2003) Probing the contribution of IKs to canine ventricular repolarization: key role for beta-adrenergic receptor stimulation. Circulation 107: 2753–2760.
89. Heijman J, Volders PG, Westra RL, Rudy Y (2011) Local control of beta-adrenergic stimulation: Effects on ventricular myocyte electrophysiology and Ca(2+)-transient. J Mol Cell Cardiol 50: 863–871.
90. Roden DM (2008) Clinical practice. Long-QT syndrome. N Engl J Med 358: 169–176.
91. Koivumaki JT, Korhonen T, Tavi P (2011) Impact of sarcoplasmic reticulum calcium release on calcium dynamics and action potential morphology in human atrial myocytes: a computational study. PLoS Comput Biol 7: e1001067.
92. Crampin EJ, Smith NP (2006) A dynamic model of excitation-contraction coupling during acidosis in cardiac ventricular myocytes. Biophys J 90: 3074–3090.
93. Livshitz L, Rudy Y (2009) Uniqueness and stability of action potential models during rest, pacing, and conduction using problem-solving environment. Biophys J 97: 1265–1276.
94. Iribe G, Kohl P, Noble D (2006) Modulatory effect of calmodulin-dependent kinase II (CaMKII) on sarcoplasmic reticulum Ca2+ handling and interval-force relations: a modelling study. Philos Transact A Math Phys Eng Sci 364: 1107–1133.
95. Ji Y, Zhao W, Li B, Desantiago J, Picht E, et al. (2006) Targeted inhibition of sarcoplasmic reticulum CaMKII activity results in alterations of Ca2+ homeostasis and cardiac contractility. Am J Physiol Heart Circ Physiol 290: H599–606.
96. Wehrens XH, Lehnart SE, Reiken SR, Marks AR (2004) Ca2+/calmodulin-dependent protein kinase II phosphorylation regulates the cardiac ryanodine receptor. Circ Res 94: e61–70.
97. Sanguinetti MC, Curran ME, Zou A, Shen J, Spector PS, et al. (1996) Coassembly of K(V)LQT1 and minK (IsK) proteins to form cardiac I(Ks) potassium channel. Nature 384: 80–83.
98. Nakajo K, Ulbrich MH, Kubo Y, Isacoff EY (2010) Stoichiometry of the KCNQ1 - KCNE1 ion channel complex. Proc Natl Acad Sci U S A 107: 18862–18867.
99. Franz MR, Swerdlow CD, Liem LB, Schaefer J (1988) Cycle length dependence of human action potential duration in vivo. Effects of single extrastimuli, sudden sustained rate acceleration and deceleration, and different steady-state frequencies. J Clin Invest 82: 972–979.
100. Pueyo E, Husti Z, Hornyik T, Baczko I, Laguna P, et al. (2010) Mechanisms of ventricular rate adaptation as a predictor of arrhythmic risk. Am J Physiol Heart Circ Physiol 298: H1577–1587.
101. Romero L, Pueyo E, Fink M, Rodriguez B (2009) Impact of ionic current variability on human ventricular cellular electrophysiology. Am J Physiol Heart Circ Physiol 297: H1436–1445.
102. Saucerman JJ, Healy SN, Belik ME, Puglisi JL, McCulloch AD (2004) Proarrhythmic consequences of a KCNQ1 AKAP-binding domain mutation: computational models of whole cells and heterogeneous tissue. Circ Res 95: 1216–1224.
103. Bernabeu MO, Bordas R, Pathmanathan P, Pitt-Francis J, Cooper J, et al. (2009) CHASTE: incorporating a novel multi-scale spatial and temporal algorithm into a large-scale open source library. Philos Transact A Math Phys Eng Sci 367: 1907–1930.
104. Ramanathan C, Jia P, Ghanem R, Ryu K, Rudy Y (2006) Activation and repolarization of the normal human heart under complete physiological conditions. Proc Natl Acad Sci U S A 103: 6309–6314.
105. Sarkar AX, Sobie EA (2010) Regression analysis for constraining free parameters in electrophysiological models of cardiac cells. PLoS Comput Biol 6: e1000914.
106. Acsai K, Kun A, Farkas AS, Fulop F, Nagy N, et al. (2007) Effect of partial blockade of the Na(+)/Ca(2+)-exchanger on Ca(2+) handling in isolated rat ventricular myocytes. Eur J Pharmacol 576: 1–6.
107. Watanabe M, Otani NF, Gilmour RF, Jr. (1995) Biphasic restitution of action potential duration and complex dynamics in ventricular myocardium. Circ Res 76: 915–921.
108. Gima K, Rudy Y (2002) Ionic current basis of electrocardiographic waveforms: a model study. Circ Res 90: 889–896.
109. Yan GX, Antzelevitch C (1996) Cellular basis for the electrocardiographic J wave. Circulation 93: 372–379.